Title

Dedifferentiation and neuronal repression define familial Alzheimer's disease

Journal

Science Advances, 6(46)

ISSN

2375-2548

Authors

Caldwell, Andrew B
Liu, Qing
Schroth, Gary P
et al.

Publication Date

2020-11-13

DOI

10.1126/sciadv.aba5933

Peer reviewed

DISEASES AND DISORDERS

Dedifferentiation and neuronal repression define familial Alzheimer's disease

Andrew B. Caldwell[1], Qing Liu[2], Gary P. Schroth[3], Douglas R. Galasko[2], Shauna H. Yuan[2]*, Steven L. Wagner[2,4], Shankar Subramaniam[1,5,6,7†]

Identifying the systems-level mechanisms that lead to Alzheimer's disease, an unmet need, is an essential step toward the development of therapeutics. In this work, we report that the key disease-causative mechanisms, including dedifferentiation and repression of neuronal identity, are triggered by changes in chromatin topology. Here, we generated human induced pluripotent stem cell (hiPSC)–derived neurons from donor patients with early-onset familial Alzheimer's disease (EOFAD) and used a multiomics approach to mechanistically characterize the modulation of disease-associated gene regulatory programs. We demonstrate that EOFAD neurons dedifferentiate to a precursor-like state with signatures of ectoderm and nonectoderm lineages. RNA-seq, ATAC-seq, and ChIP-seq analysis reveals that transcriptional alterations in the cellular state are orchestrated by changes in histone methylation and chromatin topology. Furthermore, we demonstrate that these mechanisms are observed in EOFAD-patient brains, validating our hiPSC-derived neuron models. The mechanistic endotypes of Alzheimer's disease uncovered here offer key insights for therapeutic interventions.

INTRODUCTION

Early-onset familial Alzheimer's disease (AD) (EOFAD) is a dominantly inherited neurodegenerative disorder elicited by more than 300 mutations in the *PSEN1*, *PSEN2*, and *APP* genes (*1*). Hallmark pathological changes and symptoms observed, namely, the accumulation of misfolded β-amyloid (Aβ) in plaques and Tau aggregates in neurofibrillary tangles associated with progressive memory loss and cognitive decline, are understood to be temporally accelerated manifestations of the more common sporadic late-onset AD (LOAD). The complete penetrance of EOFAD-causing mutations has allowed for experimental models, which have proven integral to the overall understanding of AD (*2*). However, the failure of pathology-targeting therapeutic development suggests that the formation of plaques and tangles may be symptomatic and not describe the etiology of the disease (*3*, *4*). In this work, we used an integrative, multiomics approach and systems-level analysis in human induced pluripotent stem cell (hiPSC)–derived neurons to generate a mechanistic disease model for EOFAD. Using patient-specific cells from donors harboring four unique mutations in *PSEN1* differentiated into neurons, we characterized the disease-related gene expression and chromatin accessibility changes by RNA sequencing (RNA-seq), assay for transposase-accessible chromatin sequencing (ATAC-seq), and histone methylation chromatin immunoprecipitation sequencing (ChIP-seq). Here, we show that the defining disease-causing mechanism of EOFAD is dedifferentiation, causing neurons to traverse the lineage-defining chromatin landscape along an alternative axis to a mixed-lineage cell state with gene signature profiles indicative of less-defined ectoderm and nonectoderm lineages via REST (RE1-Silencing Transcription factor)–mediated repression of neuronal lineage specification gene programs and the activation of nonspecific germ layer precursor gene programs concomitant with modifications in chromatin accessibility. Further, a reanalysis of existing transcriptomic data from *PSEN1*-mutant patient brain samples demonstrates that the mechanisms identified in our experimental system recapitulate EOFAD in the human brain. Our results comprise a disease model which describes the mechanisms culminating in dedifferentiation that contribute to neurodegeneration.

RESULTS

Nondemented control (NDC), $PSEN1^{M146L}$, $PSEN1^{H163R}$, $PSEN1^{A246E}$, and $PSEN1^{A431E}$ hiPSCs were generated and differentiated into neurons as previously described (*5*–*10*) (Fig. 1A and fig. S1A). Subsequent RNA-seq and differential expression analysis of $CD44^{-}/CD184^{-}$ purified neurons using the *limma* TREAT method (*11*, *12*) with a threshold of |fold change (FC)| > 1.5 and adjusted $P < 0.05$ identified 11,187 differentially expressed genes (DEGs) in $PSEN1^{M146L}$ neurons, 5443 DEGs in $PSEN1^{H163R}$ neurons, 3069 DEGs in $PSEN1^{A246E}$ neurons, and 2508 DEGs $PSEN1^{A431E}$ neurons relative to NDC with substantial overlap between all four mutations at the level of shared DEGs and shared DEG ontology (Fig. 1, B and C, and fig. S1, B and C). Quantification of Aβ38, Aβ40, and Aβ42 levels illustrates that *PSEN1* mutant neurons exhibit elevated Aβ40 and Aβ42, decreased Aβ38/Aβ42 ratios, and differential Aβ40/Aβ42 ratios relative to NDC (Fig. 1D). To characterize the functional programs modulated and to delineate the transcriptional regulators controlling them, we first carried out preranked gene set enrichment analysis (GSEA) using *fgsea* (*13*, *14*) with the Gene Ontology (GO) database, revealing consistent enrichment of gene sets related to cell cycle, pluripotency, inflammation, and nonectoderm lineage dedifferentiation (mesendoderm lineage specification captured by cardiac system–related development gene sets) with positive gene regulation, combined with consistent enrichment of gene sets related to neuron lineage specification and neuron function with negative gene regulation across all four *PSEN1*-mutant neurons (Fig. 1E). Notably, the GO biological process (GOBP) synaptic signaling gene set, among other key neuronal function–related gene sets, was identified as

[1]Department of Bioengineering, University of California, San Diego, La Jolla, CA, USA. [2]Department of Neurosciences, University of California, San Diego, La Jolla, CA, USA. [3]Illumina Inc., San Diego, CA, USA. [4]VA San Diego Healthcare System, La Jolla, CA, USA. [5]Department of Cellular and Molecular Medicine, University of California, San Diego, La Jolla, CA, USA. [6]Department of Nanoengineering, University of California, San Diego, La Jolla, CA, USA. [7]Department of Computer Science and Engineering, University of California, San Diego, La Jolla, CA, USA.
*Present address: N. Bud Grossman Center for Memory Research and Care, Department of Neurology, University of Minnesota, Minneapolis, MN, USA; GRECC, Minneapolis VA Health Care System, Minneapolis, MN, USA.
†Corresponding author. Email: shankar@ucsd.edu

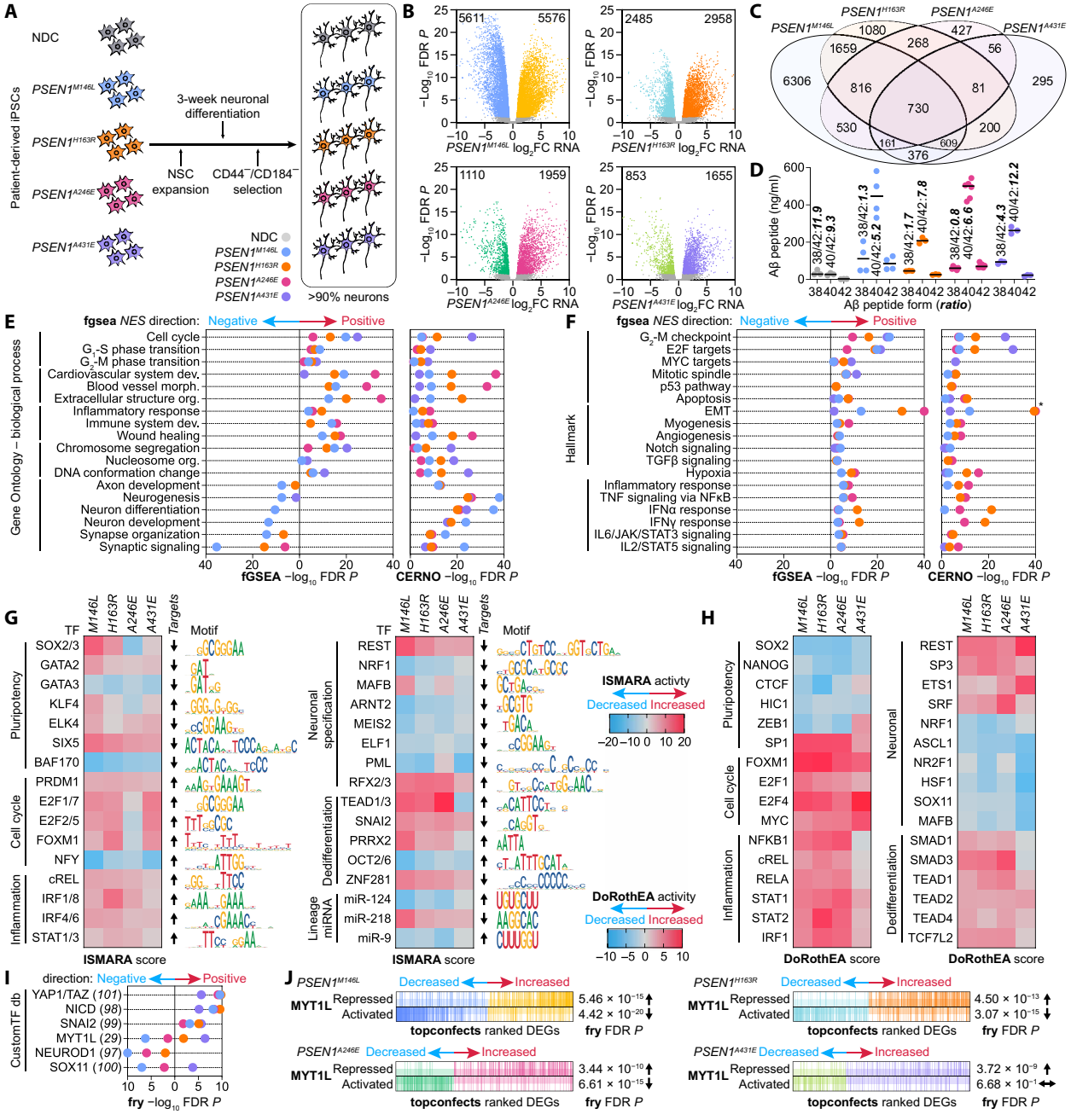

Fig. 1. *PSEN1* mutant hiPSC-derived neurons undergo dedifferentiation through the activation and repression of key endotypes. (**A**) Patient-derived NDC, *PSEN1*^{M146L}, *PSEN1*^{H163R}, *PSEN1*^{A246E}, and *PSEN1*^{A431E} hiPSCs were differentiated into neurons and purified by CD44$^-$/CD184$^-$ selection. (**B**) RNA-seq volcano plots of DEGs (Ensembl ID) in the four *PSEN1* mutations relative to NDC as determined by the *limma* TREAT method with a 1.5-fold change (FC) threshold and a false discovery rate (FDR)–adjusted $P < 0.05$. (**C**) Venn diagram overlap of DEGs across the four AD-causal *PSEN1* mutant hiPSC-derived neurons. (**D**) Aβ38, Aβ40, and Aβ42 levels across NDC and the *PSEN1* mutant neurons; numbers above indicate Aβ38/Aβ42 and Aβ40/Aβ42 ratios. (**E** and **F**) Ranked enrichment analysis of *PSEN1*^{M146L}, *PSEN1*^{H163R}, *PSEN1*^{A246E}, and *PSEN1*^{A431E} gene expression signatures using the (E) GOBP or (F) Hallmark database by the *fgsea* multilevel enrichment test (left) or *tmod* CERNO enrichment test (right); genes ranked by minimum significant difference (msd; CERNO) or signed msd (*fgsea*); *–log$_{10}$ FDR–djusted $P > 60$. (**G** and **H**) Common TFs across the *PSEN1* mutants with predicted significant activity change by (G) ISMARA motif analysis (based on *z* score, TF-gene Pearson correlation, and average gene target expression change) or (H) DoRothEA TF-gene target analysis (based on normalized enrichment score), curated into six key modulated disease-associated endotypes. ISMARA average target gene expression change indicated by up (increasing relative to NDC) or down (decreasing relative to NDC) arrows. (**I**) Common ranked enrichment analysis of *PSEN1* mutant neuron gene expression signatures using a custom-defined list of TF-gene targets using the *limma* fry test; genes ranked by *topconfects* confect ranking. (**J**) Distribution of DEGs in *PSEN1* mutant neurons ranked by *topconfects* for MYT1L-repressed (top) and MYT1L-activated (bottom) genes with corresponding enrichment statistic and direction of overall expression change (arrows) by the *limma* fry test. TF, transcription factor.

significantly enriched by the CERNO statistical test (*15*) and the *limma* fry (*16*) rotational test with negative gene regulation in all *PSEN1* mutant neurons (Fig. 1E and fig. S2A). Enrichment using the Hallmark database with *fgsea* and CERNO test confirmed the significant enrichment with positive gene regulation of cell cycle, inflammatory, and nonectoderm lineage [represented by the enrichment of epithelial-mesenchymal transition (EMT) gene set] programs observed using the GOBP databases, particularly for the $PSEN1^{A431E}$ and $PSEN1^{A246E}$ mutations (Fig. 1F). This test also revealed significant enrichment with positive gene regulation of gene sets related to Notch and transforming growth factor–β (TGFβ) signaling, which can contribute to the promotion of a nonectoderm lineage. As terminally differentiated neurons are generally thought to exist in the quiescent G_0 phase, yet these four *PSEN1* mutant neurons exhibit significant enrichment for cell cycle–related processes, we sought to determine the neuron cell cycle state. This revealed that $PSEN1^{M146L}$ and $PSEN1^{A246E}$ neuron populations have a significantly lower percentage of cells in the G_0 and S phases and a higher percentage in the G_2-M phases, suggesting that they have reentered the cell cycle (fig. S2B). To validate these results, we performed quantitative polymerase chain reaction (qPCR) in $PSEN1^{M146L}$, $PSEN1^{A246E}$, and $PSEN1^{H163R}$ hiPSC-derived neurons for key cell cycle–related and REST-repressed (*GAD1*) genes, recapitulating expression patterns observed in the corresponding RNA-seq data for each mutation (fig. S2C). To characterize the transcriptional regulation of these altered gene programs, we performed two complementary transcription-factor (TF) activity analysis approaches: motif-centric TF activity analysis by ISMARA (Integrated System for Motif Activity Response) (*17*) to characterize the TFs and microRNAs (miRNAs) whose motif activity most significantly changes between the *PSEN1* mutant and NDC neurons; and TF-gene target-centric activity analysis by DoRothEA (Discriminate Regulon Expression Analysis) (*18*), which uses the *viper* activity inference algorithm with a curated TF target regulon generated from consensus ChIP-seq, expression signatures, and TF motif studies to predict TF activity based on the directional regulation of target genes by TFs. The top transcriptional regulators identified by ISMARA motif enrichment analysis coalesced into the same general categories of disease-causal endotypes identified by ontology enrichment analysis, with consistent activation of transcriptional regulators related to pluripotency (including SOX2 and SOX3, GATA2 and GATA3, and KLF4) (*19*, *20*), cell cycle (E2F family members and FOXM1) (*21*), inflammation [interferon regulatory factor (IRF), signal transducers and activators of transcription (STAT), and nuclear factor κB (NFκB) transcriptional regulators] (*22*, *23*), and dedifferentiation (including TEAD factors, SNAI2, and PRRX2) (Fig. 1G). A substantial number of regulators controlling neuron lineage specification and neuron function were found to have differential activity, including activation of the neuron lineage repressor REST and deactivation of neuronal and mitochondrial metabolic regulators such as NRF1 (Nuclear Respiratory Factor 1) (*24*, *25*). The alternative DoRothEA approach identified significant activity change for TFs associated with the same endotypes identify by *fgsea* ontology enrichment and ISMARA analysis, with expanded activity characterization of regulators related to cell cycle activation, inflammation, dedifferentiation (SMAD and TEAD factors, and TCF7L2), and repression of neuronal lineage (deactivation of ASCL1 and SOX11) (Fig. 1H). Preranked GSEA by *fgsea* using the Encyclopedia of DNA Elements (ENCODE)–Chip-X Enrichment Analysis (ChEA) and ReMap TF databases showed analogous enrichment of cell cycle, pluripotency, nonectoderm lineage, and regulators identified by ISMARA and DoRothEA (fig. S2, D to E). Given the consistent enrichment of ontology and TF gene sets related to nonectoderm and neuronal lineage, we generated a modest custom TF database for transcriptional regulators controlling these programs from previously published ChIP-seq and motif data. Using the self-contained *fry* enrichment test, we observed significant enrichment of TFs related to dedifferentiation [YAP1 and its co-factor paralog TAZ (*WWTR1*), SNAI2, and NOTCH1(NICD)] (*26*–*28*) and neuronal specification (MYT1L, NEUROD1, and SOX11) (Fig. 1I) (*29*–*31*). As MYT1L has been previously described to function as a repressor of nonectoderm lineages and activator of neuron lineages and the target gene enrichment direction of MYT1L target genes were found to be both up-regulated ($PSEN1^{H163R}$ and $PSEN1^{A431E}$) and down-regulated ($PSEN1^{M146L}$ and $PSEN1^{A246E}$), we split the MYT1L gene set into MYT1L-activated and MYT1L-repressed and performed the *fry* enrichment test. All *PSEN1* mutants, save for the $PSEN1^{A431E}$ condition, demonstrated significant enrichment with up-regulated gene expression for MYT1L-repressed targets (containing nonectoderm lineage genes) and significant enrich with down-regulated gene expression for MYT1L-activated targets (containing neuron lineage-specifying genes) (Fig. 1J). Further, two miRNAs previously been shown to promote neuronal lineage specification as well as to repress cell cycle and nonectoderm lineage processes, miR-124 and miR-9 (*32*, *33*), were identified by ISMARA as having significant activity change and are known repressors of the most significantly activated TF identified, REST (*34*). To characterize the transcriptional regulation of these enriched gene sets, we used the miRTarBase (*35*) database to perform preranked GSEA miRNA target enrichment, revealing that the targets of functionally relevant miR-124 and miR-9 are significantly enriched with targets overall up-regulated in all four *PSEN1* mutant conditions (fig. S2F). To determine whether this is due to loss of miR-124 and miR-9, we performed miRNA-qPCR, revealing that miR-124 and miR-9 levels are significantly decreased in $PSEN1^{M146L}$ and $PSEN1^{A246E}$ neurons relative to NDC (fig. S2G), which suggests that the increased expression of miR-124 and miR-9 targets is due to derepression caused by loss of miRNA levels.

Next, we aimed to evaluate whether these observed transcriptional changes were due to modulation of the chromatin state. To this end, we performed ATAC-seq on NDC and all four *PSEN1* mutant hiPSC-derived neurons, identifying a substantial number of regions of chromatin with differential accessibility occurring within promoter and transcription start site (TSS)–associated enhancer regions in $PSEN1^{M146L}$, $PSEN1^{H163R}$, and $PSEN1^{A431E}$ neurons relative to NDC (Fig. 2, A and B, and fig. S3, A and B). To identify the TFs mechanistically associated with these differential accessible regions of chromatin, we used two approaches: HINT (Hmm-based IdeNtification of Transcription factor footprints) TF footprinting analysis (*36*, *37*) and motif enrichment analysis with GimmeMotifs (*38*). HINT analysis with the HOCOMOCOv11 (*39*) motif database identified a loss of TF footprinting activity of neuron mitochondrial regulators (NRF1, CREB1, and ATF1) (*40*) and KLF factors potentially involved in axon regeneration (*41*) across multiple *PSEN1* mutant neurons (Fig. 2C). NRF1 TF footprinting accessibility, as characterized by Tn5 transposase insertions around the NRF1 motif by HINT, revealed a correlated loss of accessibility in $PSEN1^{M146L}$, $PSEN1^{H163R}$, and $PSEN1^{A431E}$ neurons (Fig. 2D). Next, we separated differentially accessible peaks into those occurring within the gene

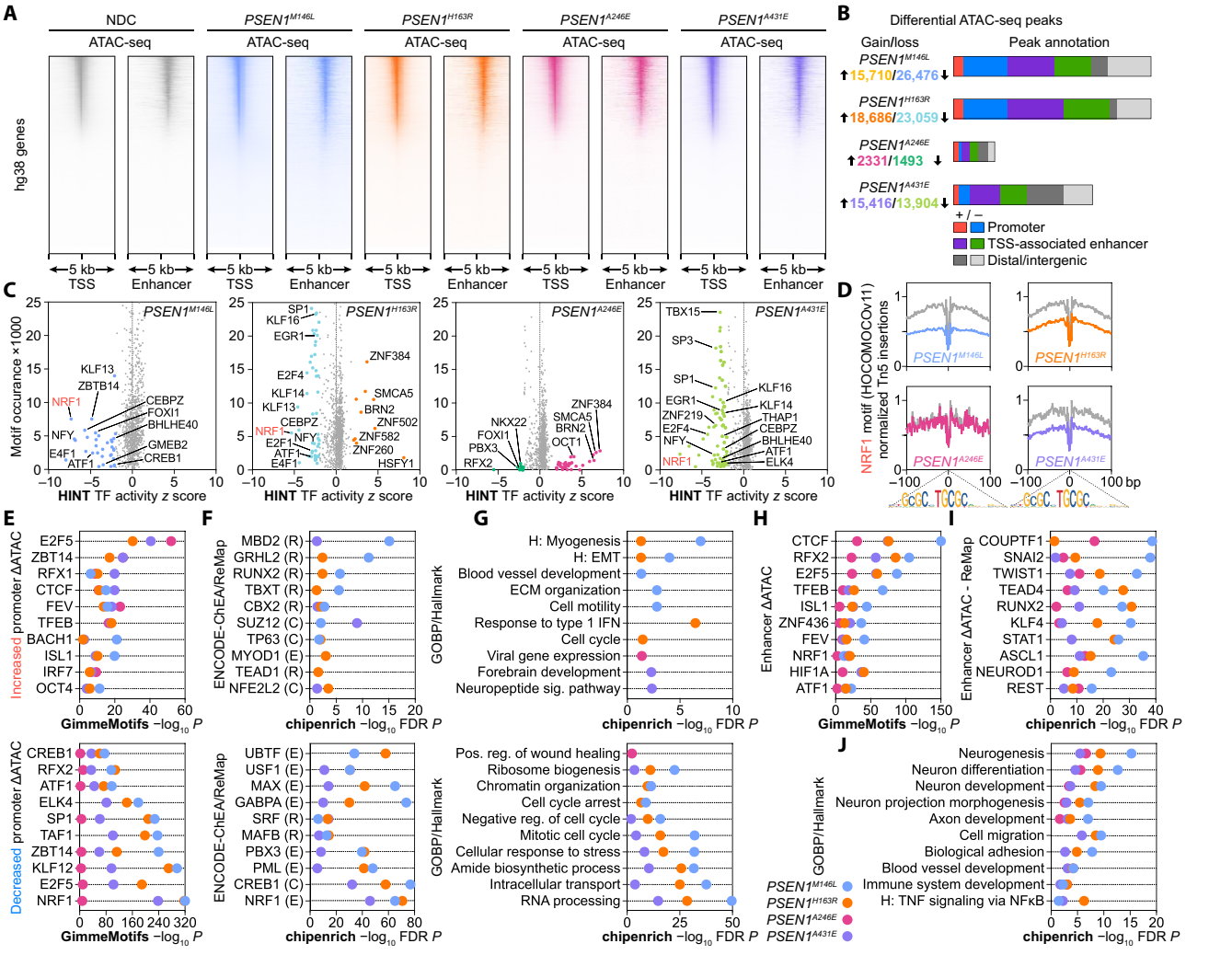

Fig. 2. Regions of differential chromatin accessibility are enriched for transcriptional regulators and pathways mirroring gene expression signatures. (**A**) TSS and TSS-associated enhancer heatmap coverage plots of Tn5-accessible chromatin in NDC, *PSEN1*^{M146L}, *PSEN1*^{H163R}, *PSEN1*^{A246E}, and *PSEN1*^{A431E} hiPSC-derived neurons as determined by ATAC-seq. (**B**) Annotation and directionality of differential ATAC-seq peaks for the four *PSEN1* mutant hiPSC-derived neurons relative to NDC. (**C**) HINT TF footprinting analysis in all differentially accessibly ATAC-seq regions using the HOCOMOCOv11 motif database to identify TFs with a change in footprinting activity. (**D**) Tn5 insertion density in each *PSEN1* mutant relative to NDC around NRF1 motifs as determined by HINT. (**E**) TF motif enrichment of promoter-associated regions with increased accessibility (top) or decreased accessibility (bottom) using GimmeMotifs and the HOCOMOCOv11 motif database. (**F** and **G**) *chipenrich* enrichment analysis of differentially accessible promoter-associated regions with increased accessibility (top) or decreased accessibility (bottom) using (F) ENCODE-ChEA consensus and ReMap TF-gene target databases (E, ENCODE; C, ChEA; R, ReMap) or (G) GOBP and Hallmark ontology databases (H, Hallmark). (**H**) TF motif enrichment of differentially accessible enhancer–associated regions using GimmeMotifs and the HOCOMOCOv11 motif database. (**I** and **J**) *chipenrich* enrichment analysis of differentially accessible enhancer–associated regions using (I) ENCODE-ChEA consensus and ReMap TF-gene target databases or (J) GOBP and Hallmark ontology databases. All results presented $P < 0.05$ (GimmeMotifs) or FDR $P < 0.05$ (HINT, chipenrich).

promoter region [−1000, +500 base pairs (bp) from TSS] or within a TSS-associated enhancer region (FANTOM5) (*42*) and performed GimmeMotifs motif enrichment with the Homer (*43*) algorithm and the HOCOMOCOv11 and SwissRegulon motif databases. This revealed significant enrichment of motifs related to cell cycle (E2F5), pluripotency (OCT4), chromatin modifications and interactions (ZBTB14 and CTCF), inflammation (IRF7), and cell damage and death associated with neurodegeneration (TFEB and BACH1) (*44*) within regions of increased accessibility with the promoter region and enrichment of neuron lineage and sensory neuron factors (RFX2 and ELK4) (*45*), neuron mitochondrial regulators (NRF1, CREB1, and ATF1), and chromatin modifiers [BAF170 (*SMARCC2*)] within regions of decreased accessibility (Fig. 2E and fig. S3, C and D). Peak enrichment using the *chipenrich* logistic regression enrichment test with the ENCODE-ChEA and ReMap TF databases revealed similar ontologies associated with the TFs identified, as nonectoderm lineage TFs (RUNX2, TBX2, MYOD1, and TEAD1) exhibited target gene enrichment within the increasing promoter peaks, while neuron-associated TFs (NRF1, CREB1, PML, and MAFB) (*46*, *47*) exhibited target gene enrichment within decreasing promoter peaks (Fig. 2F). Expanding this approach to our custom TF database revealed enrichment of motifs for Notch signaling factors, which are substrates of the gamma secretase complex (NOTCH1/NICD and RBPJ) within regions of increasing promoter chromatin accessibility and motifs

for neuronal lineage factors (RFX2, SOX11, OTX2, and NeuroD1) enriched within regions of decreasing promoter chromatin accessibility (fig. S3E). These ontological programs were also identified performing *chipenrich* using the GOBP and Hallmark gene set databases, with significant enrichment for nonectoderm lineage and cell cycle ontologies (Fig. 2G). Motif and *chipenrich* peak enrichment of enhancer-associated differential regions of accessibility identified significant enrichment of neuron lineage programs and regulatory TFs (ASCL1, NEUROD1, and REST), nonectoderm lineage programs and regulatory TFs (SNAI2, TWIST1, and RUNX2), and inflammatory processes (Fig. 2, H to J). Peak enrichment with our custom TF database revealed significant enrichment of targets of regulators involved in nonectoderm lineage and Notch signaling (YAP1, NOTCH1, and RBPJ) and both the repression (SOX9) and activation of neuronal lineage (MYT1L, SOX11, NEUROD1, and FOXP2) (fig. S3F). These results illustrate the differential accessibility occurring within neuron lineage and synaptic function genes, associated with later stages of lineage specification and function and controlled by regulators such as NRF1 and CREB1, primarily having loss of accessibility within the promoter regions, whereas genes associated with early stages of lineage definition and controlled by regulators such as REST and MYT1L-controlled genes primarily have differential accessibility within enhancer regions.

Next, we investigated regions of promoters with common differential accessibility across all four *PSEN1* mutations relative to NDC, focusing on genes related to neuron lineage and neuron function, two cellular programs significantly enriched in our RNA-seq and ATAC-seq analyses. This revealed chromatin accessibility loss in the promoters of three factors involved in controlling neuron lineage fate: *DUSP4*, *POU3F1* (OCT6), and *SOX11*; notably, OCT6 and SOX11 were predicted by our RNA-seq analysis to have significantly decreased activity in all four *PSEN1* conditions by ISMARA and DoRothEA TF activity determination approaches, respectively (Fig. 3A and fig. S4A) (*48*, *49*). Further, key synaptic function genes, such as *STXBP1*, *VGF*, and *SNAP25*, display loss of promoter accessibility with corresponding and correlated loss of gene expression relative to NDC (Fig. 3B). This accessibility loss within the promoter region was similarly observed for additional genes involved in neuron lineage specification (*BRINP1* and *CUX2*) (*50*, *51*) and synaptic function (*GABRG1*, *CNTN4*, and *BDNF*) (fig. S4, A and B). We sought to expand this approach further, finding the intersection of genes with differential accessibility and directionally correlated gene expression change. Here, we found substantial overlap of DEGs with differential accessibility under the $PSEN1^{M146L}$, $PSEN1^{H163R}$, and $PSEN1^{A431E}$ conditions (Fig. 3C). Hypergeometric enrichment analysis of the DEGs with increased expression and accessibility or decreased expression or accessibility using the ENCODE-ChEA and ReMap TF databases demonstrates the mechanistic activation of genes regulated by TFs controlling dedifferentiation (TEAD1, TWIST1, SMAD3, SALL4, and TCF7L2), nonectoderm lineage (RUNX2, TBXT, and EOMES), and pluripotency (SOX2) processes and the repression of genes regulated by TFs controlling neuron lineage and function (REST), neuron energy production (NRF1, CREB1, and NFYB), and lineage-dependent chromatin modification (PCGF2 and SUZ12) (Fig. 3, D and E). The enrichment analysis using GOBP and Hallmark mirrors these results, revealing endotype-associated activation of dedifferentiation, TGFβ signaling, and pluripotency

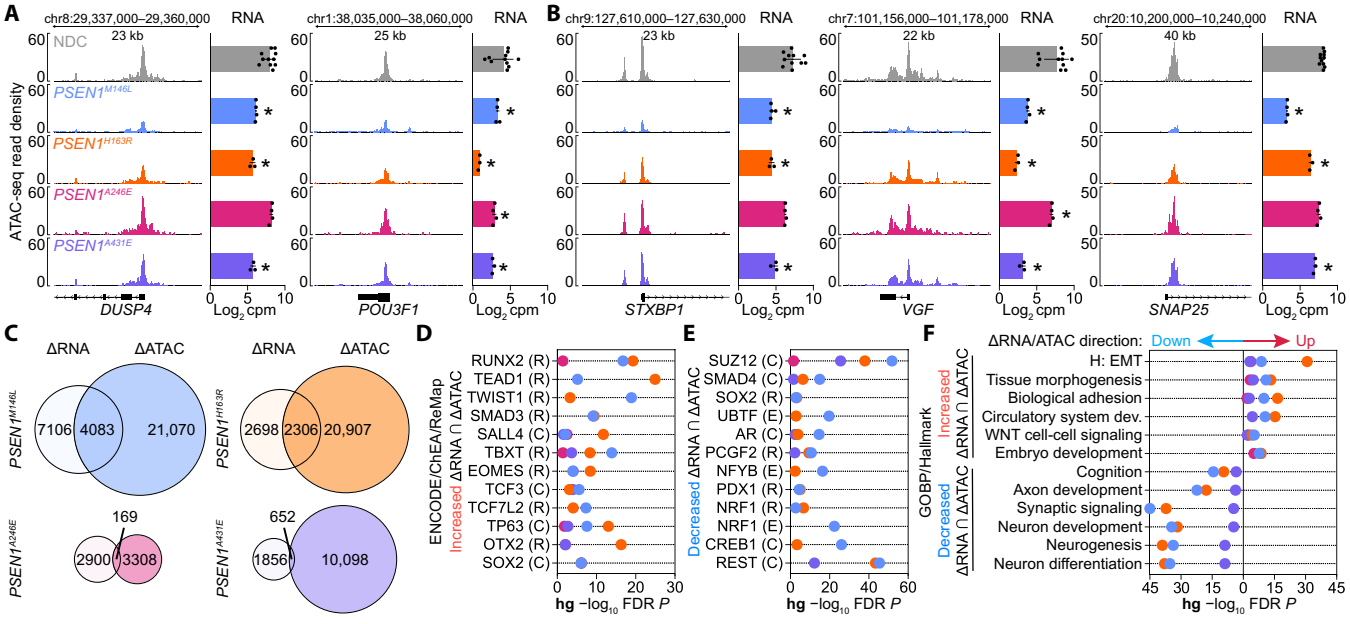

Fig. 3. Modulation of chromatin accessibility drives differential gene expression and dedifferentiation in *PSEN1* mutant hiPSC-derived neurons. (**A** and **B**) Left: Differential ATAC-seq peaks common across *PSEN1* mutant hiPSC-derived neurons occurring in the promoter regions of (A) neuronal lineage regulators or (B) synaptic function genes. Right: Corresponding gene expression of each gene for each PSEN1 condition ($PSEN1^{A246E}$, *VGF*: $\log_2$FC = −1.47, FDR $P = 5.28 \times 10^{-06}$). (**C**) Venn diagram of overlap of differential ATAC-seq peaks with corresponding directional differential gene expression change in $PSEN1^{M146L}$, $PSEN1^{H163R}$, $PSEN1^{A246E}$, and $PSEN1^{A431E}$ hiPSC-derived neurons relative to NDC (dots and error bars, replicate expression values; *DEG). (**D** and **E**) Commonly enriched terms by hypergeometric (hg) enrichment analysis using the ENCODE-ChEA consensus and ReMap TF-gene target databases for genes with correlated (D) increased or (E) decreased gene expression and chromatin accessibility. (**F**) Commonly enriched terms by hypergeometric enrichment analysis using the GOBP and Hallmark databases for genes with correlated increased (top) or decreased (bottom) gene expression and chromatin accessibility.

programs concomitant with repression of neuron lineage and synaptic function (Fig. 3F).

As chromatin accessibility can be modulated through changes in histone methylation (*52*), and TF enrichment analysis revealed gene expression loss arising from differential chromatin accessibility in NRF1- and CREB1-controlled promoter regions and REST- and histone-modulating PRC2 (polycomb repressor complex 2)–controlled target gene enhancer regions, we performed ChIP-seq on NDC and *PSEN1*^{M146L} and *PSEN1*^{A246E} hiPSC-derived neurons for the activating mark histone H3 lysine K4 trimethylation (H3K4Me3) (primarily associated with promoters) and the repressive mark histone H3 lysine K27 trimethylation (H3K27Me3) (primarily associated with polycomb repressor–controlled regions) (*53*). This revealed a substantial number of differential H3K4Me3 and H3K27Me3 peaks in both *PSEN1* conditions (Fig. 4, A and B). To investigate the potential transcriptional regulators associated with these methylation changes, we performed motif enrichment analysis of regions with an increase in activating H3KMe3 status (gain of H3KMe3 or loss of H3K27Me3) or an increase in repressive H3KMe3 (loss of H3KMe3 or gain of H3K27Me3) occurring within promoter and TSS-associated enhancer regions in *PSEN1*^{M146L} and *PSEN1*^{A246E} hiPSC-derived neurons. This identifying motifs for TFs related to cell cycle (E2F5), inflammation (IRF3), neuron lineage (NEUROD2 and PAX6), chromatin modification (EZH2 and CUX2), and neuron autophagy repression (ATF2) with an increasing in activating H3KMe3 marks and motifs for TFs related to neuron lineage (REST, RFX3, MAFB, and ELK1), neuron mitochondrial function (NRF1 and CREB1), and chromatin modification (BAF170) (Fig. 4C). These results were largely confirmed by *chipenrich* peak analysis using TF target and ontology databases, with observed increase in activating H3KMe3 status enriched for gene sets related to dedifferentiation (TWIST1, SMAD3, and SNAI2), nonectoderm lineage (RUNX2 and TBXT), pluripotency (NANOG and OCT4), and inflammation and an increase in repressive H3KMe3 status enriched for gene sets related to neuron lineage definition (REST, ASCL1, and ELF1) and neuron function (NRF1, CREB1, and FOXP2) (Fig. 4, D and E). Of these differentially methylated regions, 3429 and 1022 DEGs were found to have directionally correlated change in H3K4Me3 or H3K27Me3 status in *PSEN1*^{M146L} and *PSEN1*^{A246E} neurons, respectively (Fig. 4F). The gain of H3K4Me3 and loss of H3K27Me3 coverage or loss of H3K4Me3 and gain of H3K27Me3 coverage is apparent around genes with differential histone methylation and increased or decreased gene expression, respectively (Fig. 4G). Hypergeometric enrichment of these DEGs with differential methylation shares a similar trend with the enrichment analysis of differential methylation alone, save for the significant enrichment of cell cycle and FOXM1 target gene sets for genes with increased gene expression in the *PSEN1*^{M146L} condition (Fig. 4, H and I). These results highlight that up-regulated gene expression changes related to dedifferentiation, cell cycle, and inflammation as well as down-regulated gene expression changes related to neuron lineage and function are associated with and potentially driven by change in H3K4Me3 and H3K27Me3 at promoter and enhancer regions.

Next, we integrated the ATAC-seq data with the histone methylation ChIP-seq data, revealing that the intersection of DEGs with differential methylation concomitant with differential chromatin accessibility (Fig. 5A) showed a substantial overlap in the *PSEN1*^{M146L} condition. Moreover, the genes with increased H3K4Me3 or decreased H3K27Me3 and increased chromatin accessibility and expression are enriched for gene sets related to dedifferentiation (SMAD3 and RUNX2), nonectoderm lineage (TBX2 and MYOD1), and inflammatory gene sets in addition to pluripotency lineage factors such as GATA2, OCT4, and PRDM14, while the genes with decreased H3K4Me3 or increased H3K27Me3 and decreased chromatin accessibility and expression are enriched for gene sets related to neuron lineage and synaptic function and transcriptional control by REST, PCGF2, and PRC2 complex factors (EZH2) (Fig. 4, B and C). The mechanistic switch from differentiated to dedifferentiated neuronal state via remodeling of the chromatin state is demonstrated by the activation of transcriptional regulators controlling dedifferentiation (*TEAD2*, *SMAD3*, and *TCF7L2*) (Fig. 5D) (*54*) and the repression of transcriptional regulators controlling neuron lineage (*MYT1L* and *SOX11*) and function (*SCRT1*) (Fig. 5E) (*55*). Furthermore, the locus around the two key neuron lineage miRNAs down-regulated in *PSEN1*^{M146L} neurons, miR-9 and miR-124, show decreased chromatin accessibility and H3K4Me3 concomitant with increased H3K27Me3 (Fig. 5F). A heatmap corresponding to directionally correlated RNA expression, promoter accessibility, and H3KMe3 for an expanded list of genes belonging to the core gene programs identified here or previously identified as AD marker genes illustrates key gene expression changes occurring due to modifications of the chromatin landscape (fig. S4, C and D). The gene for the top TF with targets enriched for an increase in gene expression, chromatin accessibility, and permissive H3KMe3, the pluripotency and epigenetic regulator PRDM14, displays an increase in expression with a corresponding gain of chromatin accessibility and H3K4Me3 and loss of H3K27Me3. As REST is transcriptionally up-regulated and predicted to be activated as evidenced by ISMARA analysis and target gene repression, we carried out REST ChIP-seq in *PSEN1*^{M146L} neurons. Here, we identified 1379 REST-bound target genes, a substantial portion of which are shared with other previously reported REST target lists (fig. S5, A and B) (*56*, *57*). Furthermore, ontology enrichment analysis of these REST genes revealed significant enrichment for the canonical REST processes neuron differentiation and synapse development (fig. S5C). Enrichment analysis of these REST targets differentially expressed in *PSEN1* mutant neurons identified similar neuron lineage and function gene sets as well as dedifferentiation endotype–associated processes enriched, such as EMT and blood vessel morphogenesis (fig. S5, D and E). Overall, this multiomics, integrative analysis illustrates that REST, PRC2, MYT1L, and SOX11 neuronal target genes are primarily transcriptionally repressed because of a change in chromatin accessibility driven by modification of H3K27Me3 and H3K4Me3 status, whereas NRF1 and CREB1 neuronal target genes are significantly repressed because of loss of chromatin accessibility in the promoter without change in the H3K4Me3 or H3K27Me3 methylation state.

Patient-specific hiPSC-derived neurons are a powerful model system to investigate EOFAD-causing mutations in a mechanistic, systems-level fashion; to validate whether the mechanisms identified in *PSEN1* mutant neurons faithfully capture the disease-related processes occurring in patients with AD, we reanalyzed a previous transcriptomic study (*58*) (GSE39420) of posterior cingulate cortex brain tissue from NDC and *PSEN1* mutant (*PSEN1*^{M139T}, $n = 4$; *PSEN1*^{V89L}, $n = 2$; *PSEN1*^{E120G}, $n = 1$) EOFAD donors (fig. S6A). Expression analysis revealed a substantial number of DEGs in *PSEN1* mutant brain overlapping with *PSEN1* mutant neurons, particularly in the case of the down-regulated genes (Fig. 6A and fig. S6B). This shared gene expression signature in *PSEN1* mutant patient

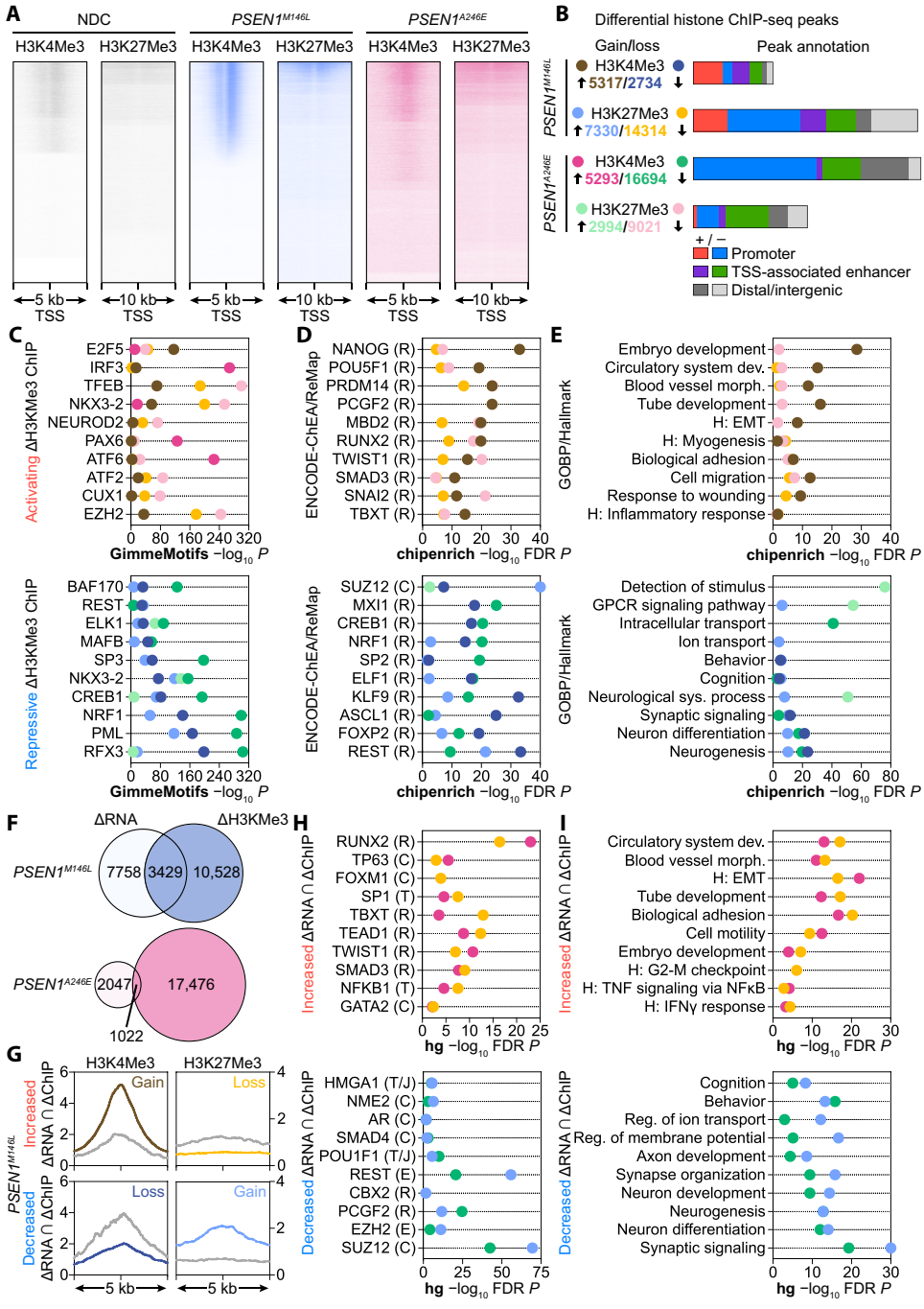

Fig. 4. Dedifferentiation in *PSEN1*^{M146L} and *PSEN1*^{A246E} hiPSC-derived neurons is caused by changes in histone methylation. (**A**) TSS heatmap coverage plots of H3K4Me3 and H3K27Me3 in NDC and *PSEN1*^{M146L} and *PSEN1*^{A246E} hiPSC-derived neurons as determined by ChIP-seq. (**B**) Annotation and directionality of differential ChIP-seq peaks in *PSEN1*^{M146L} and *PSEN1*^{A246E} hiPSC-derived neurons relative to NDC. (**C**) TF motif enrichment of regions with an increase in activating histone methylation status (increase in H3K4Me3 or decrease in H3K27Me3; top) or an increased in repressive histone methylation status (decrease in H3K4Me3 or increase in H3K27Me3; bottom) occurring within promoter or TSS-associated enhancer regions using GimmeMotifs and the HOCOMOCOv11 motif database. (**D** and **E**) *chipenrich* enrichment analysis of regions with an increase in activating histone methylation status (increase in H3K4Me3 or decrease in H3K27Me3; top) or an increased in repressive histone methylation status (decrease in H3K4Me3 or increase in H3K27Me3; bottom) occurring within promoter or TSS-associated enhancer regions using (D) ENCODE-ChEA consensus and ReMap TF-gene target databases or (E) GOBP and Hallmark ontology databases. (**F**) Venn-Euler diagram of overlap of DEGs with regions of differential H3K4Me3 or H3K27Me3 occurring within promoter or TSS-associated enhancer regions in *PSEN1*^{M146L} (top) and *PSEN1*^{A246E} (bottom) hiPSC-derived neurons. (**G**) Histone methylation density in *PSEN1*^{M146L} around DEGs with corresponding gain or loss of H3K4Me3 or H3K27Me3 status within promoter and enhancer regions. (**H** and **I**) Commonly enriched terms by hypergeometric (hg) enrichment analysis using the (H) ENCODE-ChEA Consensus, ReMap, Transfac/JASPAR (T/J), and TRRUST (T) TF-gene target databases or (I) GOBP and Hallmark databases for genes with directionally correlated increased gene expression and gain of activating H3KMe3 status (top) or decreased gene expression and gain of repressive H3KMe3 status (bottom).

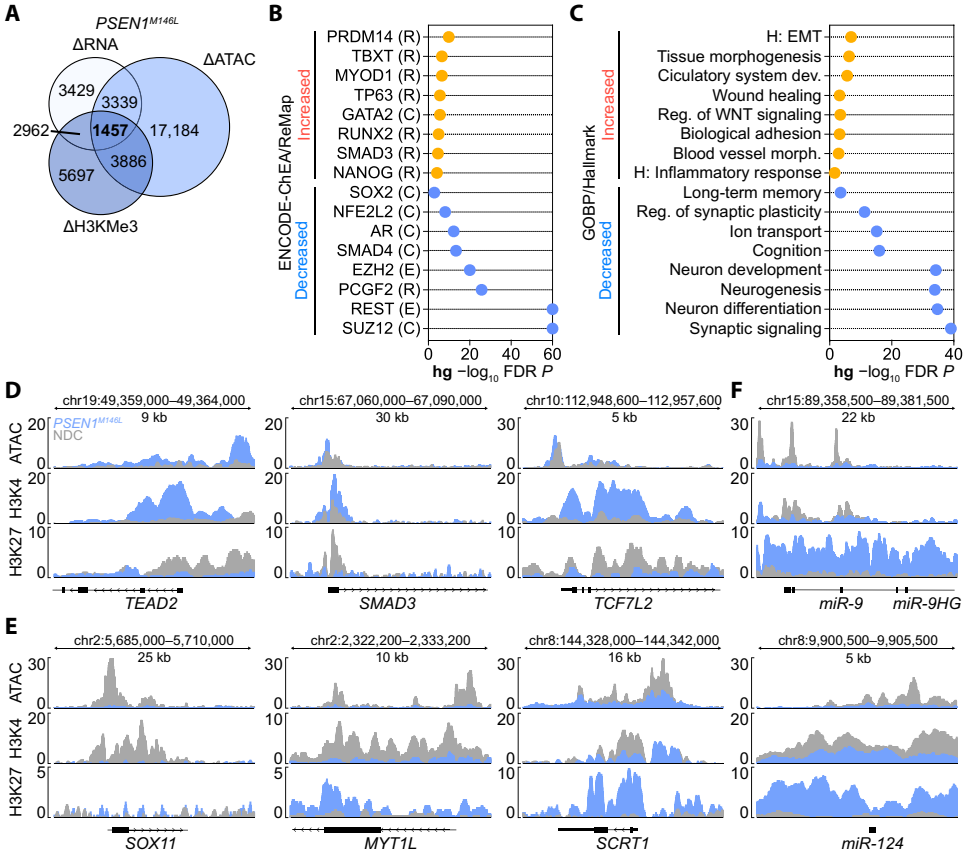

Fig. 5. Repression of neuronal lineage and function and activation of nonectoderm lineage in *PSEN1*^{M146L} hiPSC-derived neurons is orchestrated by modulation of chromatin accessibility via histone methylation. (**A**) Venn diagram of overlap of DEGs, which have intersecting and directionally corresponding change in H3K4Me3 or H3K27Me3 status flanking regions of differential accessibility occurring within gene promoters or TSS-associated enhancers in *PSEN1*^{M146L} hiPSC-derived neurons. (**B** and **C**) Hypergeometric enrichment analysis using the (B) ENCODE-ChEA consensus and ReMap TF-gene target databases or (C) GOBP and Hallmark databases for genes with increased gene expression, chromatin accessibility, and gain of activating H3KMe3 status (top; yellow) or decreased gene expression, chromatin accessibility, and gain of repressive H3KMe3 status (bottom; blue). (**D** to **F**) ATAC-seq, H3K4Me3, and H3K27Me3 read profiles around the promoter regions of (D) nonectoderm lineage–controlling TFs with increased gene expression, (E) neuronal lineage– and function-controlling TFs with decreased gene expression, or (F) lineage-defining miRNAs with decreased expression.

brain was similarly observed by transcriptional regulatory analysis approaches ISMARA (Fig. 6B) and DoRothEA (Fig. 6C), with significant activity change predicted for regulators related to neuronal differentiation (REST, PRC2 complex, and miR-124), nonectoderm lineage specification and dedifferentiation (TEAD1/3, SMAD1/3, PRRX2, and miR-124), pluripotency (GATA2), inflammation (IRF1/8 and STAT1/2/3), and cell cycle (E2F1/7, FOXM1, and miR-9) as observed in *PSEN1* mutant neurons, with REST identified as the top enriched/activated TF in *PSEN1* brain by both approaches (Fig. 6, B and C). Gene expression signature ranking of DEGs by *topconfects* for MYT1L-controlled genes in *PSEN1* human brain resemble the trend of activation of MYT1L-repressed genes and activation of MYT1L-activated genes as observed in *PSEN1* mutant neurons, suggesting that loss of MYT1L, an REST-repressed, and miR-124–promoted gene, contributes to loss of the neuronal state (Fig. 6D). Furthermore, preranked GSEA using the GOBP and Hallmark gene set databases revealed markedly similar enrichment of the six key disease-associated endotypes observed in *PSEN1* neurons, as demonstrated by the up-regulation of cell cycle, inflammation, nonectoderm lineage, and pluripotency programs and down-regulation of neuron lineage and neuron function programs (Fig. 6E).

DISCUSSION

In this work, we used a patient-specific hiPSC-derived neuron model system and an integrative multiomics approach to characterize the mechanistic changes occurring at the TF and chromatin dynamics level leading to transcriptional dysregulation in EOFAD due to *PSEN1* mutations. Expanded enrichment analysis of *PSEN1* mutant neuron transcriptomics, combined with chromatin dynamics analysis, revealed six modulated gene programs integral to the understanding of the overall disease mechanism: pluripotency, dedifferentiation, cell cycle reentry, inflammation, lineage miRNA, and neuronal specification encompassing lineage definition and synaptic function. Strikingly, all four distinct *PSEN1* mutations demonstrated consistent dysregulation of the endotypes described herein by both RNA-seq and ATAC-seq analyses, reinforcing the consistency and pervasiveness of these mechanisms to remodel the chromatin and gene expression landscape in *PSEN1*-induced EOFAD. The integration of differential RNA-seq and ATAC-seq or histone methylation ChIP-seq genes offers mechanistic insight into the type of regulatory control of these programs; for example, while the cell cycle endotype is significantly enriched in all four *PSEN1* mutants and particularly the *PSEN1*^{A431E} condition, there is less observed directional

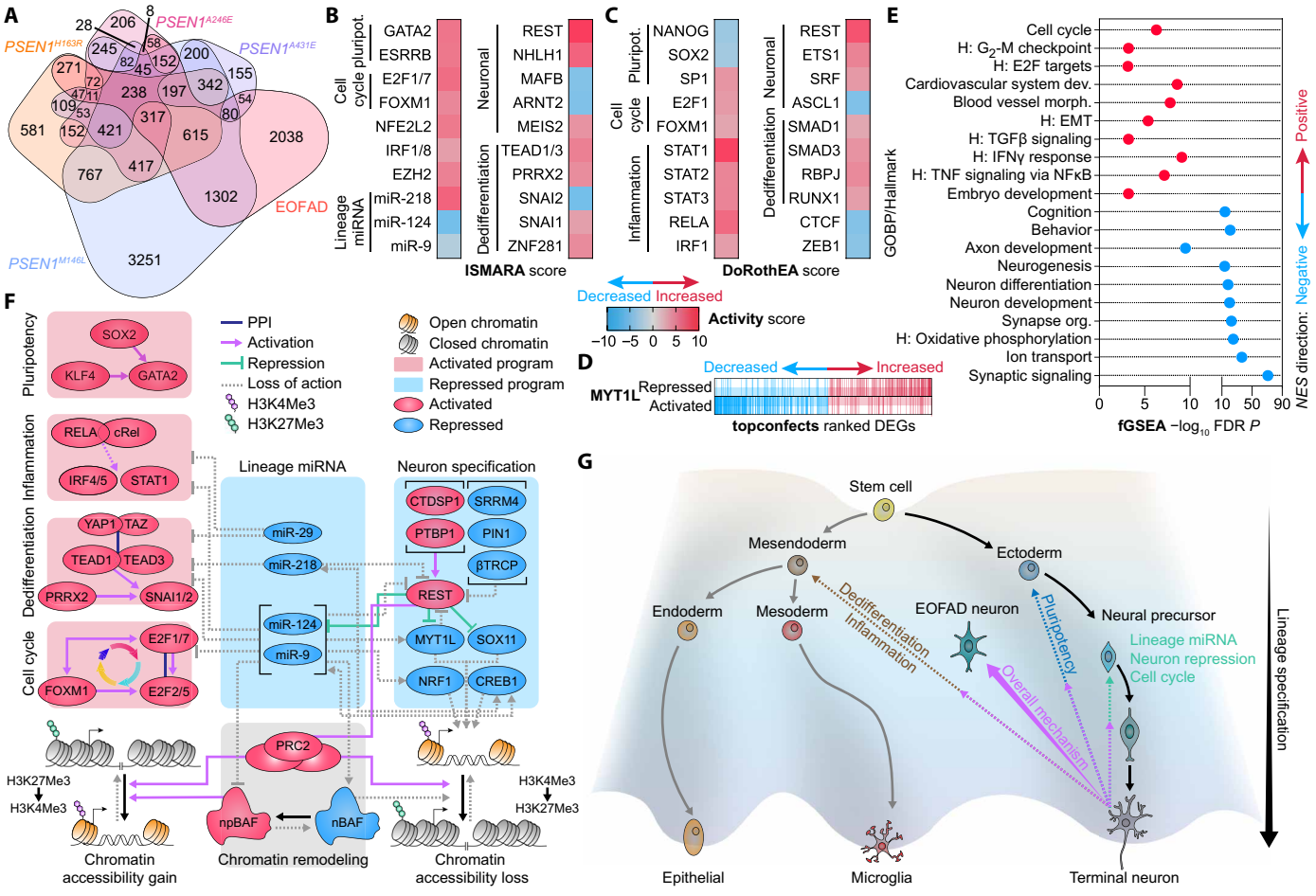

Fig. 6. Mechanisms of neuronal dedifferentiation occurring in PSEN1 hiPSC-derived neurons are observed in EOFAD patient brains. (**A**) nVenn quasi-proportional diagram of overlapping DEGs across the four AD-causal *PSEN1* mutant hiPSC-derived neurons and EOFAD patient brains. (**B** to **C**) TFs with predicted significant activity change in *PSEN1* mutant human brains by (B) ISMARA motif analysis or (C) DoRothEA TF-gene target analysis commonly enriched with *PSEN1* mutant hiPSC-derived neurons. (**D**) Distribution of DEGs in *PSEN1* mutant human brain samples ranked by *topconfects* for MYT1L-repressed (top) and MYT1L-activated (bottom) genes. (**E**) Enrichment analysis of *PSEN1* mutation human brain gene expression signatures using the GOBP and Hallmark databases by *fgsea* multilevel enrichment. (**F**) Mechanistic integration of the six disease-associated endotypes and key transcriptional regulators leading to remodeling of the chromatin state and dedifferentiation in the EOFAD disease state. (**G**) A lineage specification landscape model. Repression of neuron specification and neuron lineage miRNAs concomitant with activation of cell cycle, pluripotency, inflammation, and dedifferentiation programs revert EOFAD neurons along an alternative axis into a less differentiated, precursor state with nonectoderm lineage characteristics.

overlap between the genes belonging to cell cycle processes at the intersection of RNA-seq and ATAC-seq. This may indicate more transient gene regulatory mechanisms of cell cycle genes alternative to chromatin modification and explains why there is less observed overlap between RNA-seq and ATAC-seq in the $PSEN1^{A431E}$ condition, as this mutation has the most severe dysregulation of the cell cycle endotype among the *PSEN1* mutations studied. In contrast, the neuron lineage/synaptic function and dedifferentiation endotypes are particularly enriched at the intersection of RNA-seq and ATAC-seq approaches, suggesting that these gene expression changes are mechanistically driven by persistent changes in the chromatin landscape.

Further, the comparative enrichment for top transcriptional regulators and gene sets belonging to these endotypes across the EOFAD mutations may give insight into the documented severity of each; for example, there is evidence that the $PSEN1^{M146L}$ and $PSEN1^{A431E}$ mutants causes a particularly early onset (an average of 39 and 40 years, respectively) (*59*, *60*) along with an accelerated progression of the disease, while $PSEN1^{H163R}$ and $PSEN1^{A246E}$ mutants may have a relatively delayed onset (an average of 45 and 53 years, respectively) (*61*). Our analysis revealed that $PSEN1^{M146L}$ mutants have the most severe repression of neuronal lineage and synaptic function, whereas $PSEN1^{H163R}$ and $PSEN1^{A246E}$ mutants have the most significant up-regulation of EMT-like dedifferentiation and nonectoderm lineage, and $PSEN1^{A431E}$ is particularly enriched for cell cycle reactivation. This systems-level analysis approach categorized into disease-associated endotypes highlights the utility of using multiple, complementary enrichment approaches for the analysis of omics data: Whereas ISMARA identified the $PSEN1^{M146L}$ condition as having the most significant reactivation of the neural repressor REST, DoRothEA identified the $PSEN1^{A431E}$ as the condition with most substantially increasing REST activation, due to the differences in TF activity determination but also the definition of REST targets via motif (ISMARA) or ChIP-seq validated by motif (DoRothEA)

data. Perhaps, these key endotypes arising from our analysis of *PSEN1* mutant hiPSC-derived neurons are analogously modulated and associated with neurodegeneration in EOFAD human patient brains from alternative mutations in *PSEN1* (*PSEN1*^{M139T}, *PSEN1*^{V89L}, and *PSEN1*^{E120G}), demonstrating that these mechanisms are not unique to our hiPSC-derived neuron model system and further validating their pan-*PSEN1* mutant effect.

The integration of ATAC-seq and histone methylation ChIP-seq combined with TF target and binding site enrichment analysis of RNA-seq data in *PSEN1*^{M146L} neurons revealed that transcriptional modulation of the core gene programs have distinct mechanisms underlying the chromatin accessibility changes; whereas up-regulation of nonectoderm lineage and dedifferentiation genes and REST-mediated repression of neuronal genes occur due to changes in H3K4Me3 and H3K27Me3 status leading to changes in accessibility, the down-regulation of NRF1 and CREB1-mediated neuronal maturation and mitochondrial function genes primarily occurs due to chromatin accessibility changes within promoter regions potentially driven by alternative histone modifications combined with the loss of the pioneering TF capabilities of NRF1 and CREB1 (*62*). Analysis of promoters with differential H3K4Me3 and H3K27Me3 status revealed significant enrichment of NRF1 and CREB1, suggesting that there are additional NRF1 and CREB1 genes with promoter regions primed for chromatin accessibility loss and subsequent gene expression loss.

However, these core gene programs and the transcriptional regulators orchestrating their modulation do not exist in isolation from one another and, in certain key aspects, are intertwined in how they reshape the chromatin landscape (Fig. 4, G and H). For example, commitment to a neuron lineage involves the coordinated repression of REST, repression of the REST-recruited, histone-modifying complex PRC2, and switching of the chromatin-modulating SWI/SNF complex components from an npBAF (neuronal precursor) to an nBAF (neuronal) state, which predominantly occurs through increased expression of the CREB1-activated miRNAs miR-124 and miR-9 (*32*, *34*, *63*). miR-124 and MYT1L have been shown to restrict commitment to an neuroectoderm lineage through their repression of nonectoderm lineage genes, while miR-9 plays an integral role in the cell cycle exit required for neuronal differentiation through its repression of key cell cycle regulators upon activation (*33*). The mechanistic link between these primary transcriptional regulators and more lineage-specific secondary transcriptional regulators identified by our RNA-seq, ATAC-seq, and histone ChIP-seq highlights the hierarchical interconnection of these lineage regulators: For example, the neural-promoting TF SOX11, found to have decreased promoter chromatin accessibility and gene expression in multiple *PSEN1* mutants and enrichment with negative target gene expression by DoRothEA and *fry* enrichment tests with our custom TF database, is a REST-repressed target. Similarly, transcriptional regulators of dedifferentiation identified in our RNA-seq and ATAC-seq analyses, such as TEAD1, SNAI2, SOX9, and TWIST1, are repressed by miR-124 during neuronal differentiation (*64*). These multifaceted functions of REST, miR-124, miR-9, and MYT1L highlight their overarching identity as key neuron lineage determination factors; therefore, the combined reactivation of REST and down-regulation of miR-124, miR-9, and MYT1L cause EOFAD neurons to dedifferentiate along an alternative axis through the repression of neuronal differentiation concomitant with activation of dedifferentiation programs (Fig. 4I). Consequently, the resulting EOFAD neurons exist in a precursor-like state with transcriptional signatures of ectoderm and nonectoderm lineage alike.

While early-onset AD accounts for at most 5% of all cases, it undoubtedly shares the hallmark pathological signatures and symptoms with the late-onset, sporadic form of the disease. However, the similarities between these two forms of AD with respect to the mechanisms driving neurodegeneration occurring before the onset of pathology and cognitive decline are less well known. A previous analysis of more than 600 brains of sporadic AD patients and non-demented, age-controlled subjects identified EMT, a nonectoderm dedifferentiation process significantly enriched in our *PSEN1* mutant neurons and the *PSEN1* human brains, as the top key up-regulated gene program that facilitates the progression of healthy aging into neurodegenerative AD (*65*). miR-124 is the top enriched transcriptional regulator for the disease-contributing gene programs identified in this previous study (fig. S6B), and we found substantial gene overlap between the EMT genes dysregulated in patients with sporadic LOAD and *PSEN1* mutant neurons presented here; all four *PSEN1* mutant neurons showed significant enrichment with increased gene expression for the Alz module (*65*) of uniquely disease-associated genes (fig. S6C). Moreover, the National Institutes of Health Accelerating Medicines Partnership - Alzheimer's Disease (AMP-AD) program's Agora list of sporadic AD susceptibility genes identified by multiple omics approaches shows an overlap with EOFAD at both the gene and gene program level, with key drivers and markers of neuronal dedifferentiation, including *REST*, *HDAC1*, *ELAVL4*, *GABRA4*, *SCN2A*, and *VGF* similarly identified. This commonality of cellular programs altered in both the early-onset familial and late-onset sporadic forms offers a key insight into the underlying mechanistic basis for neurodegeneration in AD and provides a basis for innovative therapeutic intervention at an earlier state in the progression of the disease.

MATERIALS AND METHODS

hiPSC line generation

NDC, *PSEN1*^{M146L}, *PSEN1*^{H163R}, and *PSEN1*^{A431E} fibroblasts were derived from skin biopsies in accordance with University of California (UC), San Diego Institutional Review Board (IRB) approval, whereas *PSEN1*^{A246E} fibroblasts were obtained commercially (Coriell, catalog no. AG06840). The generation and characterization of the hiPSC lines were carried out as previously reported (*5*, *7*) from fibroblasts by retroviral transduction using the reprogramming factors *OCT4*, *SOX2*, *KLF4*, and *c-MYC*. These five iPSC lines were used for all downstream neuron differentiation applications.

Human neuron preparation

The protocol used for neuron preparation was previously described (*6*, *9*) with modifications. Briefly, PA6 cells were plated in a 10-cm dish and seeded with 100,000 iPSC next day. To enhance neural induction, cultures were treated with Noggin (500 ng/ml; R&D Systems) and 10 μM SB431542 (Tocris) for the first 6 days of differentiation. On day 12, neural stem cells (NSCs) were sorted using cell surface signature CD24^{+}/CD184^{+}/CD44^{-}/CD271^{-}. NSCs were expanded in NSC growth medium [DMEM/F-12, GlutaMAX (Thermo Fisher Scientific, catalog no. 10565018), 1× B-27 (Thermo Fisher Scientific, catalog no. 17504044), 1× N-2 (Thermo Fisher Scientific, catalog no. 17502001), 1× penicillin-streptomycin (Thermo Fisher Scientific, catalog no. 15070063), and human bFGF-2 (20 ng/ml;

BioPioneer, catalog no. HRP-0011)]. At 80% confluence, the medium was changed to neuron differentiation medium (DMEM:F12 + GlutaMAX, 1× B-27, 1× N-2, and 1× penicillin-streptomycin) for 3 weeks of differentiation as previously described (*8*, *9*). After differentiation, the cultures were dissociated with Accutase (Sigma-Aldrich, catalog no. A6964). Cells were resuspended in 200 μl of iMag buffer (1× neural differentiation medium, 0.5 μM EDTA, and 0.5% bovine serum albumin), followed by incubation with R-phycoerythrin (PE) mouse anti-human CD184 and CD44 antibodies (BD Biosciences, catalog nos. 561733 and 561858, respectively) for 15 min on ice in the dark. The mixture was washed with iMag buffer and subsequently incubated with anti-PE–conjugated magnetic beads (BD Biosciences) for 30 min at room temperature as previously described (*9*, *10*). Magnetic bead separation was carried out for 8 min according to the manufacturer's protocol (BD Biosciences). The supernatant containing purified $CD184^{-}/CD44^{-}$ neurons was then removed and spun down for downstream applications.

RNA-seq and data processing

For RNA-seq, total RNA from magnetically purified human NDC (replicates, $n = 8$), $PSEN1^{M146L}$ (replicates, $n = 4$), $PSEN1^{H163R}$ (replicates, $n = 3$), $PSEN1^{A246E}$ (replicates, $n = 3$), and $PSEN1^{A431E}$ (replicates, $n = 4$) hiPSC-derived neurons was prepared using the RNeasy Plus Micro Kit (QIAGEN, catalog no. 74034) according to the manufacturer's protocol. On-column deoxyribonuclease digestion was subsequently performed on total RNA extracts according to the manufacturer's recommendations to remove any genomic contamination (QIAGEN, catalog no. 79254). Libraries were prepared for RNA-seq using the TruSeq Stranded Total RNA Library Prep Kit (Illumina, catalog no. RS-122-2303) by the Ribo-Zero ribosomal RNA reduction method (Illumina, catalog no. MRZG12324). Samples were sequenced at the UC San Diego Institute for Genomics Medicine (IGM) sequencing core on an Illumina HiSeq 4000 generating paired-end, 100-bp reads with an average of 25 million reads per sample (Illumina, catalog no. FC-410-1001). We incorporated an additional hiPSC-derived neuron NDC line [Craig Venter B (CVB) line 1; replicates, $n = 3$] from a previously published study (*66*) using the same neuron differentiation method and processed the data in parallel with the data generated here.

RNA-seq data preprocessing was performed using the TrimGalore! package (*67*), removing sequencing adaptors and selecting for all paired-end reads above a quality score threshold (Phred $Q > 20$). Trimmed RNA-seq reads were mapped to the GRCh38.99 human transcriptome using kallisto v0.46.1 (*68*) with the options -bias, --rf-stranded, and -b 100, followed by transcript level summation to the gene level using the R package *tximport* v1.8.0 (*69*). Differential expression analysis was performed for all four *PSEN1* mutant iPSC-derived neurons relative to NDC using the TREAT method in the R package *limma* (*11*, *12*) with a null-hypothesis *t* test FC threshold of 1.5 and selection of DEGs with a false discovery rate (FDR)–adjusted *P* value of <0.05.

TF and miRNA activity analysis

TF activity analysis was performed using ISMARA (*17*) and DoRothEA (*18*). For ISMARA analysis, quality and adaptor trimmed fastq.gz RNA-seq files for all hiPSC-derived neurons were uploaded to ismara.unibas.ch for processing, followed by sample average. To determine a directional *z*-score for each enriched motif identified, the *z*-score for each given motif was multiplied by the sign of the Pearson correlation between each motif and its target genes and the direction of change in expression for said target genes (i.e., −1 for down-regulated genes and +1 for up-regulated genes). For motifs associated with miRNAs, qPCR expression (miR-9 and miR-124) or literature evidence (e.g., miR-218) was used to determine a positive of negative correlation with gene targets of the given motif. For DoRothEA analysis, the gene ranking for each *PSEN1* mutation relative to NDC was generated by calculating absolute value of the minimum significant distance (msd), defined as the lower bound of the 95% confidence interval of the $\log_2$FC, using the *tmodlimmaTest* function in the *tmod* (*15*) R package and multiplying by the sign of the $\log_2$FC. TF activity analysis was performed using the *msviper* function in the *viper* (*70*) R package with the DoRothEA C regulon network. TF target analysis was also performed with additional TF gene set databases: Transfac/JASPAR and ENCODE-ChEA consensus from Enrichr (*71*, *72*), incorporating the consensus genes targets identified for 104 TFs from the ENCODE project (*73*) and ChEA datasets, ReMap (*74*), and TRRUST (*75*); for miRNA target analysis, the miRTarBase v2017 (*35*) database was used. For TF target analysis of neuron-related TFs not well represented in the ISMARA database, DoRothEA regulons, or other TF databases, we generated a custom TF target database of endotype-associated TFs obtained from Gene Expression Omnibus (GEO) (data S1). ChIP-seq data for each TF were downloaded from GEO provided by the original authors, or raw sequencing data were uploaded to CRUNCH (*76*) for peak identification. Peaks were annotated with the Homer v4.10 function annotatePeaks, and each list of target genes filtered for HGNC (HUGO Gene Nomenclature Committee) protein coding genes. For the MYT1L target gene list, candidate MYT1L targets were identified using the MYT1L_200-623 primary motif from Mall *et al.* (*29*) and the Homer v4.10 (*43*) function scanMotifGenomeWide, subsequently annotated with annotatePeaks. This list of candidate genes was first filtered for HGNC protein coding genes and then further filtered for differential gene expression change upon MYT1L knockdown or overexpression previously characterized (*29*, *77*), splitting into MYT1L-repressed and MYT1L-activated gene sets. For enrichment analysis using this custom neural TF database, gene expression signatures were ranked by confect value at a FDR generated by the *topconfects* (*78*) R package and directional enrichment performed using the *fry* ranked rotational test function in *limma* with confect value serving as gene weights. The self-contained *fry* test was selected over the competitive *fgsea* test used for enrichment analysis with the publicly available TF database above due to the smaller size of our custom neural TF database.

Gene set enrichment and pathway analysis

Gene set enrichment and pathway analysis for RNA-seq was performed primarily by two complementary approaches: (i) GOBP (*79*) and Hallmark Pathway (*80*) enrichment of differential gene expression signatures using the *fgseamultilevel* function in the *fgsea* (*14*) R package and (ii) the *tmodCERNOtest* function in the *tmod* (*15*) R package. For the weighted, directional *fgsea* statistical enrichment test, genes were ranked by the directional msd statistic as described for DoRothEA analysis, while for the CERNO test, genes were ranked by msd. For miRNA target analysis, the miRTarBase v2017 database was used with both *fgsea* and a hypergeometric test of up-regulated and down-regulated DEGs using the *tmodHG* function in *tmod*. For enrichment using *fry* rotational test and GOBP gene sets, genes were ranked by confect value with *topconfects* as in enrichment analysis using our custom TF database.

ATAC-seq and data processing

ATAC-seq transposition experiments were performed as previously reported (*81*) on 50,000 NDC (replicates, $n = 5$), $PSEN1^{M146L}$ (replicates, $n = 2$), $PSEN1^{H163R}$ (replicates, $n = 3$), $PSEN1^{A246E}$ (replicates, $n = 2$), and $PSEN1^{A431E}$ (replicates, $n = 3$) hiPSC-derived neurons, using the Illumina Nextera DNA Sample Preparation Kit (Illumina, catalog no. 15028523) and the QIAGEN MinElute PCR Purification Kit (QIAGEN, catalog no. 28004). ATAC-seq libraries were generated from transposed DNA using the Kapa Biosystems Real-Time Library Amplification Kit (Kapa Biosystems, catalog no. 07959028001) according to the manufacturer's recommendations, monitoring amplification by qPCR and stopping the reaction when all samples reached a fluorescence amplification intensity between standards 1 and 3. ATAC-seq libraries were further purified using the QIAGEN MinElute PCR Purification Kit and sequenced at the UC San Diego IGM sequencing core on an Illumina HiSeq 4000 platform generating paired-end, 50-bp reads with an average of 25 million reads per sample.

ATAC-seq data preprocessing was performed with TrimGalore!, removing sequencing adaptors and selecting for all paired-end reads above a quality score threshold (Phred $Q > 20$). Trimmed reads were aligned to the GRCh38 human genome (GCA_000001405.15 with no alternative analysis) using BBMap v37.95 in the BBTools suite with the options maxindel = 20 ambig = random, followed by sorting and indexing of bam files using SAMtools v1.3 (*82*), and annotation of PCR duplicates using the Picard v2.3.0 MarkDuplicates function with the option VALIDATION_STRINGENCY = LENIENT. All duplicates and mitochondrial, chromosome X, chromosome Y, and Epstein-Barr virus (EBV) reads were removed using SAMtools v1.3 command view with the options -b -h -f 3 -F 4 -F 8 -F 256 -F 1024 -F 2048. One $PSEN1^{A246E}$ ATAC-seq sample was found to be unsuitable for further analysis, so was removed, and the other $PSEN1^{A246E}$ ATAC-seq sample was randomly subsampled into two using the SAMtools view function. To determine regions of open chromatin, i.e., those accessible by the Tn5 transposase, HMMRATAC v1.2.5 (*83*) was used to call peaks on the ATAC-seq data and determine regions of open chromatin with the options –m 50,200,400,600 --score all. The specifically called open regions of chromatin were then passed to the R package *Diffbind* v2.8.0 (*84*) to determine regions of differential accessibility between each NDC and *PSEN1* mutant conditions using the CONDITION_CONSENSUS peak selection and edgeR-block differential peak method. Differentially accessible regions of DNA were annotated using the R packages *ChIPseeker* (*85*), defining the promoter region −1000 to 500 bp from the TSS. Enhancer-associated ATAC-seq regions were defined differential peaks occurring within the region list of TSS-associated enhancers generated by the FANTOM5 project (*42*), finding the intersecting DNA regions with the join_overlap_inner function in the *plyranges* R package (*86*).

ATAC-seq enrichment analysis

To determine the TF footprints associated with the gain or loss of chromatin accessibility and motifs enriched for these regions, we used two approaches: HINT-ATAC for TF footprinting and GimmeMotifs for motif enrichment. HINT v0.12.3 (*36*, *37*) was used with the following parameters: rgt-hint function footprinting with the options --atac-seq --paired-end --organism = hg38 to identify TF footprints in each sample; rgt-motifanalysis function matching to match footprints to known TFs in the HOCOMOCO v11 (*39*) human pwm database; and rgt-hint function differential with the option --window-size 200. Differential HINT footprinting was performed for all differentially accessible regions over the entire HMMRATAC-called open chromatin region. For TF motif enrichment with GimmeMotifs (*38*), differential ATAC-seq regions were split into peaks occurring within promoters or within enhancers. The gimme motifs function was used with both the HOCOMOCOv11 (*39*) and SwissRegulon (*87*) pwm databases and the Homer (*43*) motif-finding algorithm. For enrichment analysis of differential ATAC-seq regions, we used the logistic regression model test function *chipenrich* in the *chipenrich* R package (*88*) with the locus definition *nearest_tss* for enrichment of promoter-located peaks and *1kb_outside* for enhancer-located peaks using the ENCODE-ChEA and ReMAP TF-gene target databases and GOBP and Hallmark ontology databases. Genes with differential chromatin expression were defined as those called as DEGs ($|FC| > 1.5$ and FDR $P < 0.05$) as described above and had a differentially accessible peak (passing the threshold of $|FC| > 1.5$ and FDR $P < 0.05$) occurring in a promoter or enhancer region in the corresponding direction (e.g., decreased accessibility with decreased gene expression). For TF-gene target and ontology enrichment, we performed a hypergeometric test using the *tmodHG* function in the *tmod* (*15*) R package with the ENCODE-ChEA and ReMap TF databases and the GOBP and Hallmark databases. Promoter and TSS-associated enhancer heatmaps were generated with the deepTools (*89*) functions *computeMatrix* and *plotHeatmap*. ATAC-seq coverage plots were generated in IGV v2.8.6 (*90*).

Histograms of ATAC-seq read density were generated with the Homer v4.10 function annotatePeaks. For ranking of differential accessibility within the promoter or enhancer regions of target genes of different TFs, the *confect* ranking [i.e., the $\log_2$FC value at which each ATAC-seq region achieved significant (FDR $P < 0.05$) differential accessibility] as determined by the function *edger_confects* in the *topconfects* R package was used, and distribution figures were made with the *barcodeplot* function in the *limma* R package.

Integration of RNA-seq and ATAC-seq was performed by finding all overlapping Ensembl genes with differential gene expression and differential chromatin accessibility occurring in the same direction with the threshold of $|FC| > 1.5$ and a FDR $P < 0.05$ for both RNA-seq and ATAC-seq. For enrichment analysis, the hypergeometric test in the *tmod* R package was used with the ENCODE-ChEA, ReMap, and our custom TF databases, as well as the GOBP and Hallmark gene set databases with a defined background list of all genes with a called ATAC-seq peak in each condition.

ChIP-seq and data processing

For H3K4Me3 and H3K27Me3 ChIP-seq experiments, NDC, $PSEN1^{M146L}$, and $PSEN1^{A246E}$ ($n = 1$) hiPSC-derived neurons were processed using the Active Motif ChIP-IT High Sensitivity Kit according to the manufacturer's recommendations (Active Motif, catalog no. 53040). Briefly, cells were washed with cold 1× phosphate-buffered saline (PBS) and collected in a 1.5-ml tube in PBS, followed by formaldehyde fixation for 10 min at room temperature. After addition of stop solution, cells were incubated at room temperature for 5 min and subsequently washed with 1× PBS wash buffer and resuspended in chromatin prep buffer. Following incubation on ice for 10 min, cells were lysed by performing 30 plunges in a chilled dounce homogenizer. Samples were then resuspended in Active Motif ChIP Buffer and chromatin sonication performed using a

probe tip sonicator on ice for a total of 10 min per sample (30 × 20-s intervals). Optimal sonicated chromatin fragment lengths were confirmed by agarose gel and used for immunoprecipitation (IP) reactions. Five hundred nanograms of purified, sonicated chromatin was incubated with 5 μl of H3K4Me3 (Active Motif, catalog no. 39159) or H3K27Me3 (Active Motif, catalog no. 39155) rabbit polyclonal antibody overnight at 4°C. After decrosslinking, ChIP DNA was purified using the QIAGEN MinElute PCR Purification Kit (QIAGEN, catalog no. 28004); libraries for H3K4Me3, H3K27Me3, and 1% input were generated for NDC and $PSEN1^{M146L}$ conditions at the UC San Diego IGM sequencing core using Illumina TruSeq LT adaptors (Illumina, catalog no. FC-121-2001). Sequencing was performed on an Illumina HiSeq 4000 generating single-read, 75-bp reads with an average of 20 million reads per sample.

ChIP-seq data preprocessing was performed using the BBDuk package (v37.95) in the BBTools suite, removing sequencing adaptors and selecting for all paired-end reads above a quality score threshold (Phred $Q > 10$). Trimmed ChIP-seq reads were aligned to the GRCh38 human genome (GCA_000001405.15 with no alternative analysis) using BBMap v37.95 in the BBTools suite with the options maxindel = 20 ambig = random, followed by sorting and indexing of bam files using SAMtools v1.3, annotation of PCR duplicates using Picard v2.3.0 MarkDuplicates with the option VALIDATION_STRINGENCY = LENIENT, and removal of PCR duplicates using SAMtools v1.3 (*82*) command view with the options -b -h -F 1024. Differential ChIP-seq peaks between the NDC and $PSEN1^{M146L}$ or NDC and $PSEN1^{A246E}$ conditions were identified with the sicer_df function in the *sicer2* package (*91*) with the filter threshold $|FC| > 1.5$ and a FDR $P < 0.05$. Promoter and TSS-associated enhancer annotation, motif enrichment using GimmeMotifs, TF target and ontology enrichment using *chipenrich*, and hypergeometric enrichment analysis of integrated ChIP-seq peaks and DEGs were performed as described above for ATAC-seq with the additional TRRUST and Transfac/JASPAR gene set databases. The Homer function annotatePeaks was used to generate histograms of ChIP read density at histone methylation peak centers for genes with differential expression and differential histone methylation with the options -size 5000 -hist 10.

Integration of RNA-seq and ChIP-seq was performed by finding all overlapping Ensembl genes with differential gene expression and differential H3K4Me3 or H3K27Me3 occurring in the same direction as the activating or repressing function of each histone methylation mark (e.g., increased gene expression with gain of H3K4Me3 or loss of H3K27Me3) with the threshold of $|FC| > 1.5$ and a FDR $P < 0.05$ for both RNA-seq and ChIP-seq. For enrichment analysis, the hypergeometric test in the *tmod* R package was used with the ENCODE-ChEA, ReMap, and our custom TF databases, as well as the GOBP and Hallmark gene set databases with a defined background list of all genes with a called ChIP-seq peak in each condition.

Human brain transcriptomic analysis

Microarray data corresponding to NDC and *PSEN1* mutation EOFAD human brain samples from a previously published study (*58*) were retrieved from the National Center for Biotechnology Information (NCBI) GEO database (GSE39420) as raw CEL intensity files. Thirteen samples from this dataset, all obtained from the posterior cingulate cortex region, were selected for analysis: six NDC subject brains samples and seven EOFAD brain samples from patients harboring $PSEN1^{M139T}$ (replicates, $n = 4$), $PSEN1^{V89L}$ (replicates, $n = 2$), and $PSEN1^{E120G}$ (replicates, $n = 1$) mutations. Samples were background-corrected and $\log_2$-normalized using the "RMA" function (*92*–*94*) in the *oligo* package v1.44.0 (*95*) in R. DEGs were determined using the *limma* v3.36.2 (*11*) package, selecting for genes with a FDR-adjusted P (q) < 0.05. Venn diagram overlaps of EOFAD brain DEGs with *PSEN1* mutation hiPSC-derived neurons were generated with the *nVennR* v0.2.2 package (*96*) in R. ISMARA, DoRothEA, and *fgsea* enrichment analyses were performed as described for RNA-seq data.

Quantification of Aβ levels

Aβ peptide levels were assayed as previously described (*7*). Briefly, a Meso Scale human (4G8) Aβ 3-plex ultrasensitive kit (Meso Scale Discovery, catalog no. K15141E-2) and a custom human total Aβ kit (Meso Scale Discovery, catalog no. N45CA-1) were used to assay Aβ peptides in media from sorted, purified neurons following 5 days from plating. The NDC, $PSEN1^{M146L}$, and $PSEN1^{A246E}$ Aβ quantification data presented here are from Liu *et al.* (*7*), whereas $PSEN1^{H163R}$ and $PSEN1^{A431E}$ Aβ quantification data were generated for this work.

miRNA qPCR assay

Total RNA from magnetically purified NDC, $PSEN1^{M146L}$, and $PSEN1^{A246E}$ (replicates, $n = 3$) human iPSC-derived neurons was prepared using the miRNeasy Micro Kit (QIAGEN, catalog no. 217084), on the basis of the manufacturer's procedures. complementary DNA (cDNA) was produced using the TaqMan Advanced miRNA cDNA Synthesis Kit (Life Technologies, catalog no. A28007) according to the manufacturer's instruction. Briefly, miRNA was polyadenylated at 37C for 45 min using 20 ng of total RNA in a 5-μl reaction. After heat stop of the polyadenylation reaction at 60°C for 10 min, the reaction was held on ice for 2 min. The adaptor was then ligated to the miRNAs at 16°C for 1 hour using RNA ligase in a 15-μl reaction. Next, cDNA was synthesized from the adapter-ligated miRNAs. Quantitative reverse transcription (qRT)–PCR for miRNAs was carried out using advanced TaqMan Advanced miRNA assay (Life Technologies, catalog no. A25576), with TaqMan Fast Advanced Master Mix (Life Technologies, catalog no. 4444557) and TaqMan prime probe sets for miR-124 (Hsa-miR-124-3P and 477879_mir) and miR-9 (Hsa-miR-9-5P and 478214_mir). The qRT-PCR program was as follows: 95°C for 10 min, leading to 40 cycles at 95°C for 10 min, followed by 60°C for 20 s. The $\log_2$FC for each gene was calculated by the $\Delta\Delta C_t$ method.

Cell cycle assay

Magnetically purified NDC, $PSEN1^{M146L}$, and $PSEN1^{A246E}$ (replicates, $n = 3$) human iPSC-derived neurons were plated in 96-well plates. Cells were fixed in 70% ethanol and stored at 4°C until the day of assay. Cells were stained with FxCycle Far Red Stain (Thermo Fisher Scientific, catalog no. F10348) according to the manufacturer's protocol. Stained cells were analyzed by flow cytometry using an Accuri C6 flow cytometer (BD Biosciences).

Statistical analysis

GraphPad Prism v7.0e software was used for statistical analysis to calculate either student's t test or one-way analysis of variance (ANOVA) with posttest analysis (Dunnett's multiple comparison test) for cell cycle and qPCR assays.

SUPPLEMENTARY MATERIALS

Supplementary material for this article is available at http://advances.sciencemag.org/cgi/content/full/6/46/eaba5933/DC1

View/request a protocol for this paper from *Bio-protocol*.

REFERENCES AND NOTES

1. R. E. Tanzi, The genetics of Alzheimer disease. *Cold Spring Harb. Perspect. Med.* **2**, a006296 (2012).
2. T. M. Dawson, T. E. Golde, C. Lagier-Tourenne, Animal models of neurodegenerative diseases. *Nat. Neurosci.* **21**, 1370–1379 (2018).
3. G. Chételat, Alzheimer disease: Aβ-independent processes—Rethinking preclinical AD. *Nat. Rev. Neurol.* **9**, 123–124 (2013).
4. C. Van Cauwenberghe, C. Van Broeckhoven, K. Sleegers, The genetic landscape of Alzheimer disease: Clinical implications and perspectives. *Genet. Med.* **18**, 421–430 (2016).
5. M. A. Israel, S. H. Yuan, C. Bardy, S. M. Reyna, Y. Mu, C. Herrera, M. P. Hefferan, S. Van Gorp, K. L. Nazor, F. S. Boscolo, C. T. Carson, L. C. Laurent, M. Marsala, F. H. Gage, A. M. Remes, E. H. Koo, L. S. B. Goldstein, Probing sporadic and familial Alzheimer's disease using induced pluripotent stem cells. *Nature* **482**, 216–220 (2012).
6. S. H. Yuan, J. Martin, J. Elia, J. Flippin, R. I. Paramban, M. P. Hefferan, J. G. Vidal, Y. Mu, R. L. Killian, M. A. Israel, N. Emre, S. Marsala, M. Marsala, F. H. Gage, L. S. B. Goldstein, C. T. Carson, Cell-surface marker signatures for the isolation of neural stem cells, glia and neurons derived from human pluripotent stem cells. *PLOS ONE* **6**, e17540 (2011).
7. Q. Liu, S. Waltz, G. Woodruff, J. Ouyang, M. A. Israel, C. Herrera, F. Sarsoza, R. E. Tanzi, E. H. Koo, J. M. Ringman, L. S. B. Goldstein, S. L. Wagner, S. H. Yuan, Effect of potent γ-secretase modulator in human neurons derived from multiple presenilin 1–induced pluripotent stem cell mutant carriers. *JAMA Neurol.* **71**, 1481–1489 (2014).
8. G. Woodruff, J. E. Young, F. J. Martinez, F. Buen, A. Gore, J. Kinaga, Z. Li, S. H. Yuan, K. Zhang, L. S. B. Goldstein, The presenilin-1 ΔE9 mutation results in reduced γ-secretase activity, but not total loss of PS1 function, in isogenic human stem cells. *Cell Rep.* **5**, 974–985 (2013).
9. S. H. Yuan, N. Hiramatsu, Q. Liu, X. V. Sun, D. Lenh, P. Chan, K. Chiang, E. H. Koo, A. W. Kao, I. Litvan, J. H. Lin, Tauopathy-associated PERK alleles are functional hypomorphs that increase neuronal vulnerability to ER stress. *Hum. Mol. Genet.* **27**, 3951–3963 (2018).
10. A. Knupp, S. Mishra, R. Martinez, J. E. Braggin, M. Szabo, C. Kinoshita, D. W. Hailey, S. A. Small, S. Jayadev, J. E. Young, Depletion of the AD risk gene *SORL1* selectively impairs neuronal endosomal traffic independent of amyloidogenic APP processing. *Cell Rep.* **31**, 107719 (2020).
11. M. E. Ritchie, B. Phipson, D. Wu, Y. Hu, C. W. Law, W. Shi, G. K. Smyth, *limma* powers differential expression analyses for RNA-sequencing and microarray studies. *Nucleic Acids Res.* **43**, e47 (2015).
12. D. J. McCarthy, G. K. Smyth, Testing significance relative to a fold-change threshold is a TREAT. *Bioinformatics* **25**, 765–771 (2009).
13. A. Subramanian, P. Tamayo, V. K. Mootha, S. Mukherjee, B. L. Ebert, M. A. Gillette, A. Paulovich, S. L. Pomeroy, T. R. Golub, E. S. Lander, J. P. Mesirov, Gene set enrichment analysis: A knowledge-based approach for interpreting genome-wide expression profiles. *Proc. Natl. Acad. Sci. U.S.A.* **102**, 15545–15550 (2005).
14. G. Korotkevich, V. Sukhov, A. Sergushichev, Fast gene set enrichment analysis. bioRxiv 060012 [**Preprint**]. 22 October 2019.
15. J. Weiner III, T. Domaszewska, "tmod: An R package for general and multivariate enrichment analysis" (e2420v1, PeerJ Inc., 2016); doi:10.7287/peerj.preprints.2420v1.
16. D. Wu, E. Lim, F. Vaillant, M.-L. Asselin-Labat, J. E. Visvader, G. K. Smyth, ROAST: Rotation gene set tests for complex microarray experiments. *Bioinformatics* **26**, 2176–2182 (2010).
17. P. J. Balwierz, M. Pachkov, P. Arnold, A. J. Gruber, M. Zavolan, E. van Nimwegen, ISMARA: Automated modeling of genomic signals as a democracy of regulatory motifs. *Genome Res.* **24**, 869–884 (2014).
18. L. Garcia-Alonso, C. H. Holland, M. M. Ibrahim, D. Turei, J. Saez-Rodriguez, Benchmark and integration of resources for the estimation of human transcription factor activities. *Genome Res.* **29**, 1363–1375 (2019).
19. A. Filipczyk, C. Marr, S. Hastreiter, J. Feigelman, M. Schwarzfischer, P. S. Hoppe, D. Loeffler, K. D. Kokkaliaris, M. Endele, B. Schauberger, O. Hilsenbeck, S. Skylaki, J. Hasenauer, K. Anastassiadis, F. J. Theis, T. Schroeder, Network plasticity of pluripotency transcription factors in embryonic stem cells. *Nat. Cell Biol.* **17**, 1235–1246 (2015).
20. A. M. Gomes, I. Kurochkin, B. Chang, M. Daniel, K. Law, N. Satija, A. Lachmann, Z. Wang, L. Ferreira, A. Ma'ayan, B. K. Chen, D. Papatsenko, I. R. Lemischka, K. A. Moore, C.-F. Pereira, Cooperative transcription factor induction mediates hemogenic reprogramming. *Cell Rep.* **25**, 2821–2835.e7 (2018).
21. S. Sadasivam, J. A. DeCaprio, The DREAM complex: Master coordinator of cell cycle dependent gene expression. *Nat. Rev. Cancer* **13**, 585–595 (2013).
22. V. F.-S. Shih, R. Tsui, A. Caldwell, A. Hoffmann, A single NFκB system for both canonical and non-canonical signaling. *Cell Res.* **21**, 86–102 (2011).
23. K. Honda, A. Takaoka, T. Taniguchi, Type I inteferon gene induction by the interferon regulatory factor family of transcription factors. *Immunity* **25**, 349–360 (2006).
24. N. Ballas, C. Grunseich, D. D. Lu, J. C. Speh, G. Mandel, REST and its corepressors mediate plasticity of neuronal gene chromatin throughout neurogenesis. *Cell* **121**, 645–657 (2005).
25. S. S. Dhar, M. T. T. Wong-Riley, Coupling of energy metabolism and synaptic transmission at the transcriptional level: Role of nuclear respiratory factor 1 in regulating both cytochrome c oxidase and NMDA glutamate receptor subunit genes. *J. Neurosci.* **29**, 483–492 (2009).
26. S. Lamouille, J. Xu, R. Derynck, Molecular mechanisms of epithelial–mesenchymal transition. *Nat. Rev. Mol. Cell Biol.* **15**, 178–196 (2014).
27. M. Higuchi, T. Kato, S. Yoshida, H. Ueharu, N. Nishimura, Y. Kato, PRRX1- and PRRX2-positive mesenchymal stem/progenitor cells are involved in vasculogenesis during rat embryonic pituitary development. *Cell Tissue Res.* **361**, 557–565 (2015).
28. C. Stein, A. F. Bardet, G. Roma, S. Bergling, I. Clay, A. Ruchti, C. Agarinis, T. Schmelzle, T. Bouwmeester, D. Schübeler, A. Bauer, YAP1 exerts its transcriptional control via TEAD-mediated activation of enhancers. *PLOS Genet.* **11**, e1005465 (2015).
29. M. Mall, M. S. Kareta, S. Chanda, H. Ahlenius, N. Perotti, B. Zhou, S. D. Grieder, X. Ge, S. Drake, C. E. Ang, B. M. Walker, T. Vierbuchen, D. R. Fuentes, P. Brennecke, K. R. Nitta, A. Jolma, L. M. Steinmetz, J. Taipale, T. C. Südhof, M. Wernig, Myt1l safeguards neuronal identity by actively repressing many non-neuronal fates. *Nature* **544**, 245–249 (2017).
30. D. J. Dennis, S. Han, C. Schuurmans, bHLH transcription factors in neural development, disease, and reprogramming. *Brain Res.* **1705**, 48–65 (2019).
31. M. Bergsland, M. Werme, M. Malewicz, T. Perlmann, J. Muhr, The establishment of neuronal properties is controlled by Sox4 and Sox11. *Genes Dev.* **20**, 3475–3486 (2006).
32. A. S. Yoo, B. T. Staahl, L. Chen, G. R. Crabtree, MicroRNA-mediated switching of chromatin-remodelling complexes in neural development. *Nature* **460**, 642–646 (2009).
33. A. Shenoy, R. H. Blelloch, Regulation of microRNA function in somatic stem cell proliferation and differentiation. *Nat. Rev. Mol. Cell Biol.* **15**, 565–576 (2014).
34. J. Wu, X. Xie, Comparative sequence analysis reveals an intricate network among *REST*, *CREB* and miRNA in mediating neuronal gene expression. *Genome Biol.* **7**, R85 (2006).
35. S.-D. Hsu, F.-M. Lin, W.-Y. Wu, C. Liang, W.-C. Huang, W.-L. Chan, W.-T. Tsai, G.-Z. Chen, C.-J. Lee, C.-M. Chiu, C.-H. Chien, M.-C. Wu, C.-Y. Huang, A.-P. Tsou, H.-D. Huang, miRTarBase: A database curates experimentally validated microRNA–target interactions. *Nucleic Acids Res.* **39**, D163–D169 (2011).
36. E. G. Gusmao, M. Allhoff, M. Zenke, I. G. Costa, Analysis of computational footprinting methods for DNase sequencing experiments. *Nat. Methods* **13**, 303–309 (2016).
37. Z. Li, M. H. Schulz, T. Look, M. Begemann, M. Zenke, I. G. Costa, Identification of transcription factor binding sites using ATAC-seq. *Genome Biol.* **20**, 45 (2019).
38. S. J. van Heeringen, G. J. C. Veenstra, GimmeMotifs: A *de novo* motif prediction pipeline for ChIP-sequencing experiments. *Bioinformatics* **27**, 270–271 (2011).
39. I. V. Kulakovskiy, I. E. Vorontsov, I. S. Yevshin, R. N. Sharipov, A. D. Fedorova, E. I. Rumynskiy, Y. A. Medvedeva, A. Magana-Mora, V. B. Bajic, D. A. Papatsenko, F. A. Kolpakov, V. J. Makeev, HOCOMOCO: Towards a complete collection of transcription factor binding models for human and mouse via large-scale ChIP-seq analysis. *Nucleic Acids Res.* **46**, D252–D259 (2018).
40. B. E. Lonze, D. D. Ginty, Function and regulation of CREB family transcription factors in the nervous system. *Neuron* **35**, 605–623 (2002).
41. D. L. Moore, M. G. Blackmore, Y. Hu, K. H. Kaestner, J. L. Bixby, V. P. Lemmon, J. L. Goldberg, KLF family members regulate intrinsic axon regeneration ability. *Science* **326**, 298–301 (2009).
42. R. Andersson, C. Gebhard, I. Miguel-Escalada, I. Hoof, J. Bornholdt, M. Boyd, Y. Chen, X. Zhao, C. Schmidl, T. Suzuki, E. Ntini, E. Arner, E. Valen, K. Li, L. Schwarzfischer, D. Glatz, J. Raithel, B. Lilje, N. Rapin, F. O. Bagger, M. Jørgensen, P. R. Andersen, N. Bertin, O. Rackham, A. M. Burroughs, J. K. Baillie, Y. Ishizu, Y. Shimizu, E. Furuhata, S. Maeda, Y. Negishi, C. J. Mungall, T. F. Meehan, T. Lassmann, M. Itoh, H. Kawaji, N. Kondo, J. Kawai, A. Lennartsson, C. O. Daub, P. Heutink, D. A. Hume, T. H. Jensen, H. Suzuki, Y. Hayashizaki, F. Müller; The FANTOM Consortium, A. R. R. Forrest, P. Carninci, M. Rehli, A. Sandelin, An atlas of active enhancers across human cell types and tissues. *Nature* **507**, 455–461 (2014).
43. S. Heinz, C. Benner, N. Spann, E. Bertolino, Y. C. Lin, P. Laslo, J. X. Cheng, C. Murre, H. Singh, C. K. Glass, Simple combinations of lineage-determining transcription factors prime *cis*-regulatory elements required for macrophage and B cell identities. *Mol. Cell* **38**, 576–589 (2010).
44. C. J. Cortes, A. R. La Spada, TFEB dysregulation as a driver of autophagy dysfunction in neurodegenerative disease: Molecular mechanisms, cellular processes, and emerging therapeutic opportunities. *Neurobiol. Dis.* **122**, 83–93 (2019).

45. J. Schwartzentruber, S. Foskolou, H. Kilpinen, J. Rodrigues, K. Alasoo, A. J. Knights, M. Patel, A. Goncalves, R. Ferreira, C. L. Benn, A. Wilbrey, M. Bictash, E. Impey, L. Cao, S. Lainez, A. J. Loucif, P. J. Whiting; HIPSCI Consortium, A. Gutteridge, D. J. Gaffney, Molecular and functional variation in iPSC-derived sensory neurons. *Nat. Genet.* **50**, 54–61 (2018).
46. T. Regad, C. Bellodi, P. Nicotera, P. Salomoni, The tumor suppressor regulates cell fate in the developing neocortex. *Nat. Neurosci.* **12**, 132–140 (2009).
47. W.-M. Yu, J. M. Appler, Y.-H. Kim, A. M. Nishitani, J. R. Holt, L. V. Goodrich, A Gata3–Mafb transcriptional network directs post-synaptic differentiation in synapses specialized for hearing. *eLife* **2**, e01341 (2013).
48. S. Y. Kim, Y.-M. Han, M. Oh, W.-K. Kim, K.-J. Oh, S. C. Lee, K.-H. Bae, B.-S. Han, DUSP4 regulates neuronal differentiation and calcium homeostasis by modulating ERK1/2 phosphorylation. *Stem Cells Dev.* **24**, 686–700 (2015).
49. Q. Zhu, L. Song, G. Peng, N. Sun, J. Chen, T. Zhang, N. Sheng, W. Tang, C. Qian, Y. Qiao, K. Tang, J.-D. J. Han, J. Li, N. Jing, The transcription factor Pou3f1 promotes neural fate commitment via activation of neural lineage genes and inhibition of external signaling pathways. *eLife* **3**, e02224 (2014).
50. P. Garcia-Gutierrez, F. Juarez-Vicente, D. J. Wolgemuth, M. Garcia-Dominguez, Pleiotrophin antagonizes Brd2 during neuronal differentiation. *J. Cell Sci.* **127**, 2554–2564 (2014).
51. A. Iulianella, M. Sharma, M. Durnin, G. B. Vanden Heuvel, P. A. Trainor, *Cux2* (*Cutl2*) integrates neural progenitor development with cell-cycle progression during spinal cord neurogenesis. *Development* **135**, 729–741 (2008).
52. A. J. Bannister, T. Kouzarides, Regulation of chromatin by histone modifications. *Cell Res.* **21**, 381–395 (2011).
53. K. Hyun, J. Jeon, K. Park, J. Kim, Writing, erasing and reading histone lysine methylations. *Exp. Mol. Med.* **49**, e324 (2017).
54. L. M. Iyer, S. Nagarajan, M. Woelfer, E. Schoger, S. Khadjeh, M. P. Zafiriou, V. Kari, J. Herting, S. T. Pang, T. Weber, F. S. Rathjens, T. H. Fischer, K. Toischer, G. Hasenfuss, C. Noack, S. A. Johnsen, L. C. Zelarayán, A context-specific cardiac β-catenin and GATA4 interaction influences TCF7L2 occupancy and remodels chromatin driving disease progression in the adult heart. *Nucleic Acids Res.* **46**, 2850–2867 (2018).
55. T. Matsuda, T. Irie, S. Katsurabayashi, Y. Hayashi, T. Nagai, N. Hamazaki, A. M. D. Adefuin, F. Miura, T. Ito, H. Kimura, K. Shirahige, T. Takeda, K. Iwasaki, T. Imamura, K. Nakashima, Pioneer factor NeuroD1 rearranges transcriptional and epigenetic profiles to execute microglia-neuron conversion. *Neuron* **101**, 472–485.e7 (2019).
56. S. Rockowitz, W.-H. Lien, E. Pedrosa, G. Wei, M. Lin, K. Zhao, H. M. Lachman, E. Fuchs, D. Zheng, Comparison of REST Cistromes across human cell types reveals common and context-specific functions. *PLOS Comput. Biol.* **10**, e1003671 (2014).
57. J.-I. Satoh, N. Kawana, Y. Yamamoto, ChIP-seq data mining: Remarkable differences in NRSF/REST target genes between human ESC and ESC-derived neurons. *Bioinform. Biol. Insights.* **7**, 357–368 (2013).
58. A. Antonell, A. Lladó, J. Altirriba, T. Botta-Orfila, M. Balasa, M. Fernández, I. Ferrer, R. Sánchez-Valle, J. L. Molinuevo, A preliminary study of the whole-genome expression profile of sporadic and monogenic early-onset Alzheimer's disease. *Neurobiol. Aging* **34**, 1772–1778 (2013).
59. C. A. Mangone, E. M. Castaño, E. Levy, G. Abiusi, T. Wisniewski, M. R. Marques, E. Faccio, P. B. Gorelick, B. Frangione, R. E. Sica, Early onset Alzheimer's disease in a South American pedigree from Argentina. *Acta Neurol. Scand.* **91**, 6–13 (1995).
60. R. A. Santos-Mandujano, N. S. Ryan, L. Chávez-Gutiérrez, C. Sánchez-Torres, M. A. Meraz-Ríos, Clinical association of white matter hyperintensities localization in a mexican family with spastic paraparesis carrying the PSEN1 A431E mutation. *J. Alzheimers Dis.* **73**, 1075–1083 (2020).
61. R. Sherrington, E. I. Rogaev, Y. Liang, E. A. Rogaeva, G. Levesque, M. Ikeda, H. Chi, C. Lin, G. Li, K. Holman, T. Tsuda, L. Mar, J. F. Foncin, A. C. Bruni, M. P. Montesi, S. Sorbi, I. Rainero, L. Pinessi, L. Nee, I. Chumakov, D. Pollen, A. Brookes, P. Sanseau, R. J. Polinsky, W. Wasco, H. A. Da Silva, J. L. Haines, M. A. Perkicak-Vance, R. E. Tanzi, A. D. Roses, P. E. Fraser, J. M. Rommens, P. H. St George-Hyslop, Cloning of a gene bearing missense mutations in early-onset familial Alzheimer's disease. *Nature* **375**, 754–760 (1995).
62. R. I. Sherwood, T. Hashimoto, C. W. O'Donnell, S. Lewis, A. A. Barkal, J. P. van Hoff, V. Karun, T. Jaakkola, D. K. Gifford, Discovery of directional and nondirectional pioneer transcription factors by modeling DNase profile magnitude and shape. *Nat. Biotechnol.* **32**, 171–178 (2014).
63. S. W. Lee, Y. M. Oh, Y.-L. Lu, W. K. Kim, A. S. Yoo, MicroRNAs overcome cell fate barrier by reducing EZH2-controlled REST stability during neuronal conversion of human adult fibroblasts. *Dev. Cell* **46**, 73–84.e7 (2018).
64. Y. Sun, Z.-M. Luo, X.-M. Guo, D.-F. Su, X. Liu, An updated role of microRNA-124 in central nervous system disorders: A review. *Front. Cell. Neurosci.* **9**, 193 (2015).
65. A. A. Podtelezhnikov, K. Q. Tanis, M. Nebozhyn, W. J. Ray, D. J. Stone, A. P. Loboda, Molecular insights into the pathogenesis of Alzheimer's Disease and its relationship to normal aging. *PLOS ONE* **6**, e29610 (2011).
66. A. Almenar-Queralt, D. Merkurjev, H. S. Kim, M. Navarro, Q. Ma, R. S. Chaves, C. Allegue, S. P. Driscoll, A. G. Chen, B. Kohlnhofer, L. K. Fong, G. Woodruff, C. Mackintosh, D. Bohaciakova, M. Hruska-Plochan, T. Tadokoro, J. E. Young, N. E. Hajj, M. Dittrich, M. Marsala, L. S. B. Goldstein, I. Garcia-Bassets, Chromatin establishes an immature version of neuronal protocadherin selection during the naive-to-primed conversion of pluripotent stem cells. *Nat. Genet.* **51**, 1691–1701 (2019).
67. M. Martin, Cutadapt removes adapter sequences from high-throughput sequencing reads. *EMBnet.journal* **17**, 10–12 (2011).
68. N. L. Bray, H. Pimentel, P. Melsted, L. Pachter, Near-optimal probabilistic RNA-seq quantification. *Nat. Biotechnol.* **34**, 525–527 (2016).
69. C. Soneson, M. I. Love, M. D. Robinson, Differential analyses for RNA-seq: Transcript-level estimates improve gene-level inferences. *F1000Research.* **4**, 1521 (2016).
70. M. J. Alvarez, Y. Shen, F. M. Giorgi, A. Lachmann, B. B. Ding, B. H. Ye, A. Califano, Functional characterization of somatic mutations in cancer using network-based inference of protein activity. *Nat. Genet.* **48**, 838–847 (2016).
71. E. Y. Chen, C. M. Tan, Y. Kou, Q. Duan, Z. Wang, G. V. Meirelles, N. R. Clark, A. Ma'ayan, Enrichr: Interactive and collaborative HTML5 gene list enrichment analysis tool. *BMC Bioinformatics* **14**, 128 (2013).
72. M. V. Kuleshov, M. R. Jones, A. D. Rouillard, N. F. Fernandez, Q. Duan, Z. Wang, S. Koplev, S. L. Jenkins, K. M. Jagodnik, A. Lachmann, M. G. McDermott, C. D. Monteiro, G. W. Gundersen, A. Ma'ayan, Enrichr: A comprehensive gene set enrichment analysis web server 2016 update. *Nucleic Acids Res.* **44**, W90–W97 (2016).
73. C. A. Sloan, E. T. Chan, J. M. Davidson, V. S. Malladi, J. S. Strattan, B. C. Hitz, I. Gabdank, A. K. Narayanan, M. Ho, B. T. Lee, L. D. Rowe, T. R. Dreszer, G. Roe, N. R. Podduturi, F. Tanaka, E. L. Hong, J. M. Cherry, ENCODE data at the ENCODE portal. *Nucleic Acids Res.* **44**, D726–D732 (2016).
74. J. Chèneby, M. Gheorghe, M. Artufel, A. Mathelier, B. Ballester, ReMap 2018: An updated atlas of regulatory regions from an integrative analysis of DNA-binding ChIP-seq experiments. *Nucleic Acids Res.* **46**, D267–D275 (2018).
75. H. Han, J.-W. Cho, S. Lee, A. Yun, H. Kim, D. Bae, S. Yang, C. Y. Kim, M. Lee, E. Kim, S. Lee, B. Kang, D. Jeong, Y. Kim, H.-N. Jeon, H. Jung, S. Nam, M. Chung, J.-H. Kim, I. Lee, TRRUST v2: An expanded reference database of human and mouse transcriptional regulatory interactions. *Nucleic Acids Res.* **46**, D380–D386 (2018).
76. S. Berger, M. Pachkov, P. Arnold, S. Omidi, N. Kelley, S. Salatino, E. van Nimwegen, Crunch: Integrated processing and modeling of ChIP-seq data in terms of regulatory motifs. *Genome Res.* **29**, 1164–1177 (2019).
77. A. Yokoyama, K. Igarashi, T. Sato, K. Takagi, M. Otsuka I, Y. Shishido, T. Baba, R. Ito, J. Kanno, Y. Ohkawa, K.-I. Morohashi, A. Sugawara, Identification of myelin transcription factor 1 (MyT1) as a subunit of the neural cell type-specific lysine-specific demethylase 1 (LSD1) complex. *J. Biol. Chem.* **289**, 18152–18162 (2014).
78. P. F. Harrison, A. D. Pattison, D. R. Powell, T. H. Beilharz, Topconfects: A package for confident effect sizes in differential expression analysis provides a more biologically useful ranked gene list. *Genome Biol.* **20**, 67 (2019).
79. M. Ashburner, C. A. Ball, J. A. Blake, D. Botstein, H. Butler, J. M. Cherry, A. P. Davis, K. Dolinski, S. S. Dwight, J. T. Eppig, M. A. Harris, D. P. Hill, L. Issel-Tarver, A. Kasarskis, S. Lewis, J. C. Matese, J. E. Richardson, M. Ringwald, G. M. Rubin, G. Sherlock, Gene Ontology: Tool for the unification of biology. *Nat. Genet.* **25**, 25–29 (2000).
80. D. Croft, G. O'Kelly, G. Wu, R. Haw, M. Gillespie, L. Matthews, M. Caudy, P. Garapati, G. Gopinath, B. Jassal, S. Jupe, I. Kalatskaya, S. Mahajan, B. May, N. Ndegwa, E. Schmidt, V. Shamovsky, C. Yung, E. Birney, H. Hermjakob, P. D'Eustachio, L. Stein, Reactome: A database of reactions, pathways and biological processes. *Nucleic Acids Res.* **39**, D691–D697 (2011).
81. J. D. Buenrostro, P. G. Giresi, L. C. Zaba, H. Y. Chang, W. J. Greenleaf, Transposition of native chromatin for fast and sensitive epigenomic profiling of open chromatin, DNA-binding proteins and nucleosome position. *Nat. Methods* **10**, 1213–1218 (2013).
82. H. Li, B. Handsaker, A. Wysoker, T. Fennell, J. Ruan, N. Homer, G. Marth, G. Abecasis, R. Durbin; 1000 Genome Project Data Processing Subgroup, The sequence alignment/map format and SAMtools. *Bioinformatics* **25**, 2078–2079 (2009).
83. E. D. Tarbell, T. Liu, HMMRATAC: A hidden markov modeleR for ATAC-seq. *Nucleic Acids Res.* **47**, e91 (2019).
84. C. S. Ross-Innes, R. Stark, A. E. Teschendorff, K. A. Holmes, H. R. Ali, M. J. Dunning, G. D. Brown, O. Gojis, I. O. Ellis, A. R. Green, S. Ali, S.-F. Chin, C. Palmieri, C. Caldas, J. S. Carroll, Differential oestrogen receptor binding is associated with clinical outcome in breast cancer. *Nature* **481**, 389–393 (2012).
85. G. Yu, L.-G. Wang, Q.-Y. He, ChIPseeker: An R/Bioconductor package for ChIP peak annotation, comparison and visualization. *Bioinformatics* **31**, 2382–2383 (2015).
86. S. Lee, D. Cook, M. Lawrence, plyranges: A grammar of genomic data transformation. *Genome Biol.* **20**, 4 (2019).
87. M. Pachkov, P. J. Balwierz, P. Arnold, E. Ozonov, E. van Nimwegen, SwissRegulon, a database of genome-wide annotations of regulatory sites: Recent updates. *Nucleic Acids Res.* **41**, D214–D220 (2013).

88. R. P. Welch, C. Lee, P. M. Imbriano, S. Patil, T. E. Weymouth, R. A. Smith, L. J. Scott, M. A. Sartor, ChIP-Enrich: Gene set enrichment testing for ChIP-seq data. *Nucleic Acids Res.* **42**, e105 (2014).
89. F. Ramírez, D. P. Ryan, B. Grüning, V. Bhardwaj, F. Kilpert, A. S. Richter, S. Heyne, F. Dündar, T. Manke, deepTools2: A next generation web server for deep-sequencing data analysis. *Nucleic Acids Res.* **44**, W160–W165 (2016).
90. H. Thorvaldsdóttir, J. T. Robinson, J. P. Mesirov, Integrative Genomics Viewer (IGV): High-performance genomics data visualization and exploration. *Brief. Bioinform.* **14**, 178–192 (2013).
91. C. Zang, D. E. Schones, C. Zeng, K. Cui, K. Zhao, W. Peng, A clustering approach for identification of enriched domains from histone modification ChIP-Seq data. *Bioinformatics* **25**, 1952–1958 (2009).
92. B. M. Bolstad, R. A. Irizarry, M. Åstrand, T. P. Speed, A comparison of normalization methods for high density oligonucleotide array data based on variance and bias. *Bioinformatics* **19**, 185–193 (2003).
93. R. A. Irizarry, B. Hobbs, F. Collin, Y. D. Beazer-Barclay, K. J. Antonellis, U. Scherf, T. P. Speed, Exploration, normalization, and summaries of high density oligonucleotide array probe level data. *Biostatistics* **4**, 249–264 (2003).
94. R. A. Irizarry, B. M. Bolstad, F. Collin, L. M. Cope, B. Hobbs, T. P. Speed, Summaries of Affymetrix GeneChip probe level data. *Nucleic Acids Res.* **31**, e15 (2003).
95. B. S. Carvalho, R. A. Irizarry, A framework for oligonucleotide microarray preprocessing. *Bioinformatics* **26**, 2363–2367 (2010).
96. J. G. Pérez-Silva, M. Araujo-Voces, V. Quesada, nVenn: Generalized, quasi-proportional Venn and Euler diagrams. *Bioinformatics* **34**, 2322–2324 (2018).
97. A. Pataskar, J. Jung, P. Smialowski, F. Noack, F. Calegari, T. Straub, V. K. Tiwari, NeuroD1 reprograms chromatin and transcription factor landscapes to induce the neuronal program. *EMBO J.* **35**, 24–45 (2016).
98. M. P. White, C. V. Theodoris, L. Liu, W. J. Collins, K. W. Blue, J. H. Lee, X. Meng, R. C. Robbins, K. N. Ivey, D. Srivastava, NOTCH1 regulates matrix gla protein and calcification gene networks in human valve endothelium. *J. Mol. Cell. Cardiol.* **84**, 13–23 (2015).
99. A. M. Tsankov, H. Gu, V. Akopian, M. J. Ziller, J. Donaghey, I. Amit, A. Gnirke, A. Meissner, Transcription factor binding dynamics during human ES cell differentiation. *Nature* **518**, 344–349 (2015).
100. M. Bergsland, D. Ramsköld, C. Zaouter, S. Klum, R. Sandberg, J. Muhr, Sequentially acting Sox transcription factors in neural lineage development. *Genes Dev.* **25**, 2453–2464 (2011).
101. F. Zanconato, M. Forcato, G. Battilana, L. Azzolin, E. Quaranta, B. Bodega, A. Rosato, S. Bicciato, M. Cordenonsi, S. Piccolo, Genome-wide association between YAP/TAZ/TEAD and AP-1 at enhancers drives oncogenic growth. *Nat. Cell Biol.* **17**, 1218–1227 (2015).
102. Y. Zhou, B. Zhou, L. Pache, M. Chang, A. H. Khodabakhshi, O. Tanaseichuk, C. Benner, S. K. Chanda, Metascape provides a biologist-oriented resource for the analysis of systems-level datasets. *Nat. Commun.* **10**, 1523 (2019).

Acknowledgments: We thank K. Jepsen and the UC San Diego IGM for assistance with the sequencing performed in this research and M. Pachkov at the University of Basel for assistance with ISMARA data processing. **Funding:** This study was supported by the Alzheimer's Association New Investigator Research Award (NIRG-14-322164) (to S.H.Y.); NIH grants P50 AGO5131 (to D.R.G.), U01 NS 074501-05 (to S.L.W.), R01 LM012595 (to S.S.), U01 CA198941 (to S.S.), U01 DK097430 (to S.S.), R01 HD084633 (to S.S.), and R01 HL106579-07 (to S.S.); NSF grant STC CCF-0939370 (to S.S.); Veterans Affairs RR&D 1I01RX002259 (to S.L.W.); and Cure Alzheimer's Fund (CAF) grants (to S.L.W.). **Author contributions:** A.B.C. performed the RNA-seq, ChIP-seq, and ATAC-seq experiments, carried out the data processing and systems analysis of the RNA-seq, ChIP-seq, and ATAC-seq experiments, developed the mechanistic framework, and wrote the manuscript with contributions to Materials and Methods from other authors. A.B.C. and S.S. were involved in the characterization of the mechanisms and networks associated with EOFAD. S.H.Y. was involved in the design of hiPSC differentiation into neurons and the validation experiments along with S.L.W. and S.S. Q.L., supervised by S.H.Y., carried out the hiPSC-neuron preparation, RNA isolation, qPCR validation, Aβ peptide quantitation, and cell cycle assay experiments. G.P.S. contributed to the RNA-seq, ChIP-seq, and ATAC-seq. D.R.G. was involved in part of the study design. S.S. was involved in the overall study design, analysis, and revisions of the manuscript. **Competing interests:** The authors declare that they have no competing interests. The contents do not represent the views of the U.S. Department of Veterans Affairs or the U.S. government. **Data and materials availability:** All data needed to evaluate the conclusions in the paper are present in the paper and/or the Supplementary Materials. All sequencing presented in this work is available at the NCBI GEO under the SuperSeries accession GSE123998, encompassing RNA-seq (GSE123891), ATAC-seq (GSE123997), and ChIP-seq (GSE123884) datasets. Additional data related to this paper may be requested from the authors.

Submitted 16 December 2019
Accepted 23 September 2020
Published 13 November 2020
10.1126/sciadv.aba5933

Citation: A. B. Caldwell, Q. Liu, G. P. Schroth, D. R. Galasko, S. H. Yuan, S. L. Wagner, S. Subramaniam, Dedifferentiation and neuronal repression define familial Alzheimer's disease. *Sci. Adv.* **6**, eaba5933 (2020).